

Developments in Oxide Fiber Composites

Frank W. Zok[†]

Materials Department, University of California, Santa Barbara, California 93106

Prospects for revolutionary design of future power generation systems are contingent on the development of durable high-performance ceramic composites. With recent discoveries in materials and manufacturing concepts, composites with all-oxide constituents have emerged as leading candidates, especially for components requiring a long service life in oxidizing environments. Their insertion into engineering systems is imminent. The intent of this article is to present a synopsis of the current understanding of oxide composites as well as to identify outstanding issues that require resolution for successful implementation. Emphasis is directed toward material systems and microstructural concepts that lead to high toughness and long-term durability. These include: the emergence of La monazite and related compounds as fiber-coating materials, the introduction of the porous-matrix concept as an alternative to fiber coatings, and novel strategies for enabling damage tolerance while retaining long-term morphological stability. Additionally, materials and mechanics models that provide insights into material design, morphology evolution, and composite properties are reviewed.

I. Introduction

THE demand for high-temperature thermostructural materials continues to grow, fueled principally by power generation systems for aircraft engines, land-based turbines, rockets, and, most recently, hypersonic missiles and flight vehicles. Typical components include combustors, nozzles, and thermal insulation. With their high melting point, strength, and toughness, continuous-fiber ceramic composites (CFCCs) offer the greatest potential for enabling elevations in the operating temperatures of these systems.

Over the past 2 decades, the vast majority of CFCC research has focused on SiC–SiC systems. The supporting manufacturing technology has reached a high level of sophistication and maturity. Large components are routinely manufactured and have been tested in turbine engines and burner rigs.

Notwithstanding this progress, the long-term durability of SiC–SiC composites continues to be plagued by two persistent problems. (i) In combustion environments that contain water vapor, recession occurs by volatilization of the silica scale.^{1–3} Environmental barrier coatings must then be used in order to achieve minimum durability goals in practical designs. (ii) Although presently of secondary concern, long-standing problems with oxidation embrittlement at intermediate temperatures remain unresolved. These deficiencies have spurred interest and developments in all-oxide CFCCs. Indeed, oxide systems have emerged as leading contenders for applications requiring long service lives ($>10^4$ h) in oxidizing environments.

High toughness in CFCCs is achieved by one of three microstructural design paths (Fig. 1). All seek to promote uncorrelated fiber failure, resulting in high fiber bundle strength and energy dissipation during subsequent pullout. The most common approach uses a fiber coating that either forms a weak interface with the fibers or has an inherently low fracture toughness (Fig. 1(b)). It has been utilized extensively in SiC/SiC, C/SiC, and C/C fiber composites, principally through C and BN coatings.⁴ Similar mechanisms can be enabled through the use of fine-scale matrix porosity, obviating the need for a fiber coating (Fig. 1(c)).^{5–15} To ensure durability, the matrix must be phase compatible with the fibers, because of their intimate contact in the absence of a coating. Additionally, the pore structure must be retained at the targeted use temperature. The third approach uses fugitive coatings: ones that are volatilized by oxidation after composite fabrication, leaving a narrow gap at the fiber–matrix boundary (Fig. 1(d)).^{16–18} The present article highlights the most significant developments in the implementation of these design strategies for oxide CFCCs.

Among commercially available oxide fibers, preference has been given to two specific types: (i) Nextel™ 610—a polycrystalline, small-diameter (10 μm) alumina fiber, with high strength to 1000°–1100°C; and (ii) Nextel™ 720—a polycrystalline mulite/alumina fiber with a somewhat lower strength at ambient and moderately elevated temperatures (relative to 610), but with superior creep resistance and microstructural stability at high temperatures, to about 1200°C.¹⁹ Although most activities in high-performance oxide CFCCs have focused on these, some concept demonstrations have used large diameter ($>100 \mu\text{m}$) sapphire and eutectic alloys. The latter are not amenable to weaving and remain too expensive to find widespread use in the foreseeable future. Brief references to fiber types are included in this article. However, the status of oxide fibers is beyond the scope of this paper.

D. Green—contributing editor

Manuscript No. 22223. Received August 8, 2006; approved September 7, 2006.

This work was supported by the Air Force Office of Scientific Research (award number F49550-05-1-0134), monitored by Dr. B. L. Lee.

[†]Author to whom correspondence should be addressed. e-mail: zok@engineering.ucsb.edu

Feature

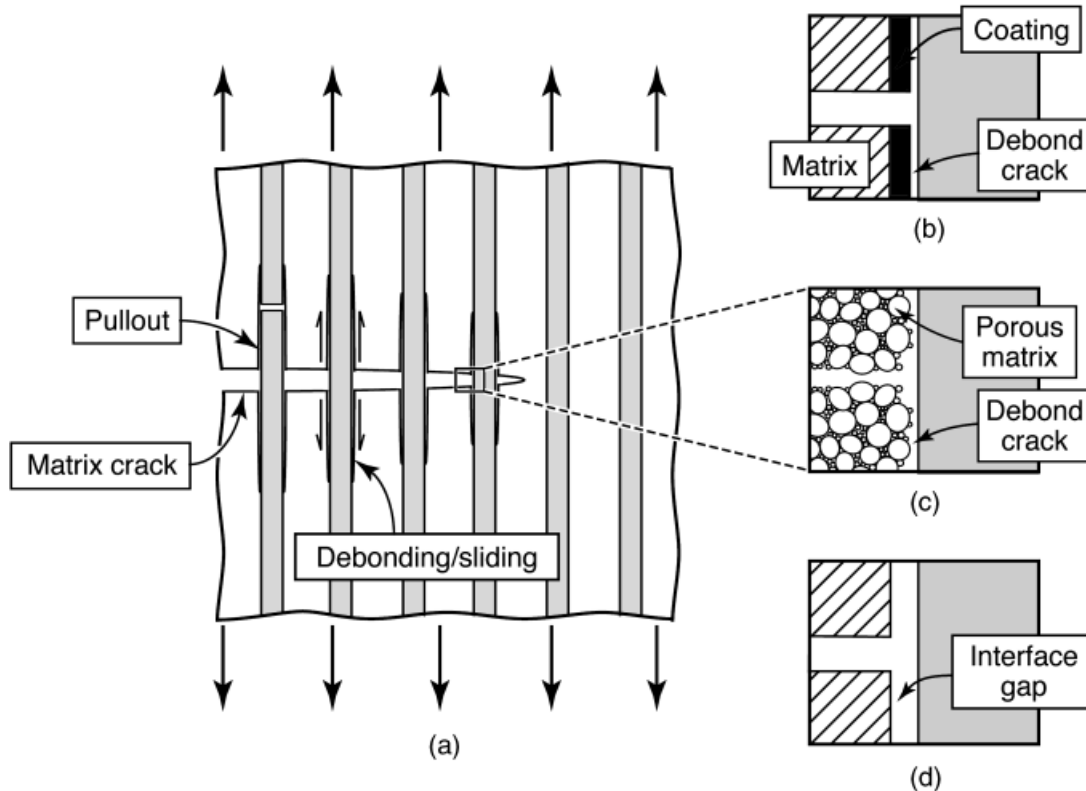


Fig. 1. Microstructural concepts for enabling crack deflection in continuous-fiber ceramic composites.

II. Developments in Fiber Coatings

(1) Monazite

Undoubtedly, the most significant development in fiber coatings has been the discovery that rare-earth phosphates such as La-monazite bond weakly to other oxides.^{20–22} In addition to forming low-toughness interfaces, monazite is non-toxic; insoluble in water, acids, and bases; does not decompose up to its melting point ($>2000^{\circ}\text{C}$); and is not easily reducible below 1400°C . In addition, it has anomalously low hardness (relative to other refractory ceramics), thereby facilitating plastic deformation during fiber–matrix sliding.^{23,24} Concurrent with the development of monazite, other mixed-oxide compounds (niobates, tungstates, and vanadates) have been pursued as candidate coating materials,^{25–27} although none exhibits a spectrum of properties to rival that of monazite.

The monazite discovery proved pivotal in the resurgence of oxide CFCCs. During the past decade, the most substantive ad-

vancements in the underpinning science and technology have been made by investigators at the U.S. Air Force Research Laboratory and at Rockwell Scientific (formerly Rockwell Science Center, where the monazite discovery was made). Numerous scientific and engineering challenges have been identified and addressed. The key developments and outstanding issues follow.

Among the numerous recipes for monazite coatings, the most promising uses rhabdophane ($\text{LaPO}_4 \cdot 1/2\text{H}_2\text{O}$) sols derived from $\text{La}(\text{NO}_3)_3$ and H_3PO_4 .^{28–30} To mitigate the deleterious effects of nitric acid (a by-product of the reaction that forms monazite), the sols are repeatedly washed in de-ionized water before application. Otherwise, significant reductions in fiber strength are obtained following coating (Fig. 2).

In one successful implementation, the coating is applied by passing continuous tows through the sol, with an immiscible liquid used to minimize bridging between coated fibers.^{31,32} The fibers are then passed through an in-line furnace (typically at $900^{\circ}\text{--}1200^{\circ}\text{C}$) and spooled. Both Nextel™ 610 and Nextel™ 720 fibers endure this process with negligible strength loss.³⁰ In its present form, this coating method is restricted to individual tows. Thus, to make useful shapes, the fibers must be first coated in tow form and subsequently woven into the desired architecture. The drawback is that the weaving can damage the coating: a consequence of the weak interfacial bond.

The thermochemical compatibility of monazite with a wide range of oxide fibers has been definitively demonstrated. For virtually all systems of interest (including Nextel™ 610 and 720, sapphire, single-crystal mullite, and $\text{Al}_2\text{O}_3/\text{ZrO}_2$ and $\text{Al}_2\text{O}_3/\text{yttrium aluminum garnet}$ eutectics), interfaces with monazite are sufficiently weak to allow debonding to occur when cracks approach from within the monazite (Fig. 3),³³ even when the residual radial compressive stresses are large (Fig. 4).²⁴ However, the resistance to subsequent sliding appears to be considerably higher than that of C- or BN-coated fibers in SiC-based CFCCs. Sliding stresses of the former systems are typically in the range of 130–250 MPa, dependent on the thermal expansion coefficients of the three constituents as well as the radial misfit strain produced by surface roughness when sliding occurs (Fig. 5).

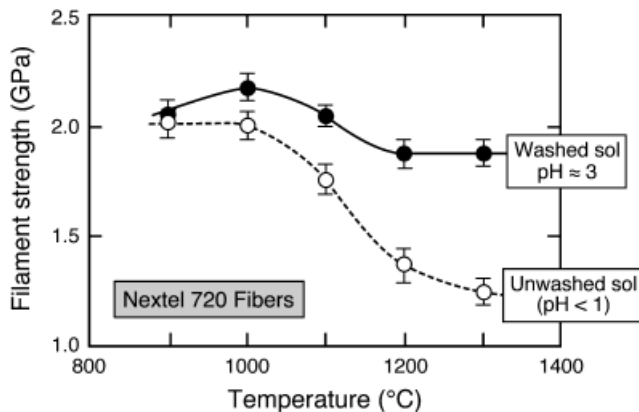


Fig. 2. Effects of heat-treatment temperature on the strength of Nextel™ 720 fibers after coating with either washed or unwashed rhabdophane sols. (Adapted from Hay and Boakye²⁹).

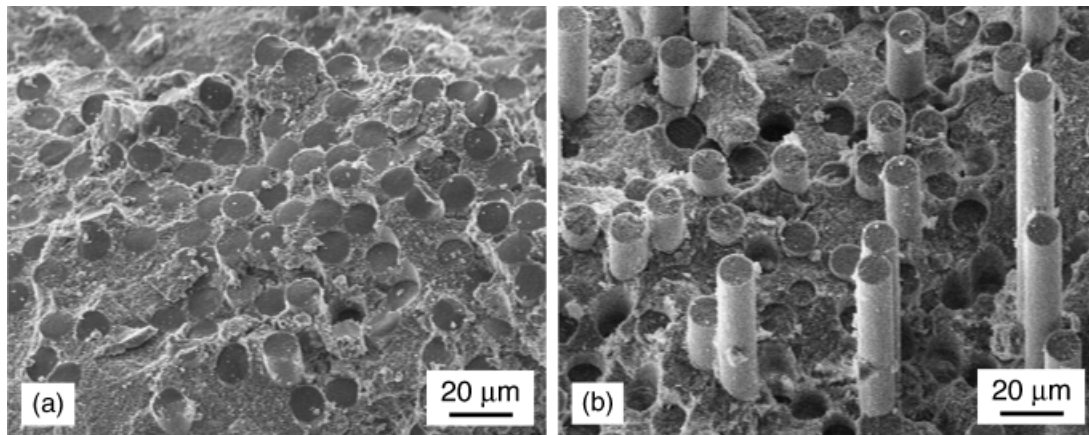


Fig. 3. Fracture surfaces of an alumina/alumina continuous-fiber ceramic composite after 5 h of exposure at 1200°C: (a) uncoated fibers, (b) monazite-coated fibers.³³ (Courtesy Kristin Keller, AFRL. Reprinted with permission).

Although the low hardness of monazite (5 GPa²⁰) facilitates plastic accommodation of the misfit, the coating is less effective than C or BN in mitigating these stresses. In the latter, the low radial stiffness of the coatings allows for elastic accommodation of the misfit with only moderate radial pressure and hence low sliding stress.

Three outstanding issues remain. (i) Presently, there is no established method for coating woven fiber cloths or preforms (distinct from tows). Such capability would circumvent the problems of weaving coated tows. (ii) The sliding stress of monazite-coated fibers in dense ceramic matrices is considerably higher than that in C- and BN-coated CFCCs, by as much as an order of magnitude. If excessively high, this may compromise composite toughness. Relative to SiC-SiC composites, more attention must be directed to thermal expansion mismatch and surface roughness effects in the oxide systems. (iii) Although the issue of fiber strength retention has been addressed, an assessment of the efficacy of monazite coating on Nextel™ 720 fibers (the highest temperature commercially available oxide fiber) has yet to be demonstrated. It will likely require the use of a mullite-based matrix, to minimize residual stress and allow fiber sliding subsequent to debonding, while retaining chemical compatibility with the fibers. The large difference in thermal expansion coefficients of alumina ($\sim 8 \times 10^{-6} \text{ K}^{-1}$) and 720 fibers ($6 \times 10^{-6} \text{ K}^{-1}$) precludes the use of alumina-rich compositions as matrix choices.

(2) Fugitive Coatings

Application of fugitive coatings to oxide CFCCs has received surprisingly little attention. Carbon appears to be the best

option. It can be deposited readily onto tows or woven fabric by chemical vapor deposition or through pyrolysis of organic precursors and is readily oxidized at moderately high temperatures.^{16,17} Although straightforward in principle, the approach has two potential drawbacks: (i) matrix sintering treatments must be performed in an inert (non-oxidizing) environment, and (ii) once the coating is oxidized, the fibers are unprotected from the surrounding matrix and may be susceptible to bonding at contact points.

Preliminary feasibility studies have yielded encouraging results. When carbon-coated Nextel™ 720 fibers were embedded in a dense calcium aluminosilicate matrix and the carbon subsequently oxidized, significant enhancements in fiber pullout were obtained.¹⁷ The retention in properties following high-temperature exposure was also improved. A more recent investigation has also shown the benefits of combining fugitive coatings with porous matrices.³⁴ For this purpose, composites were fabricated by infiltration of a mullite-20% alumina slurry into a carbon-coated Nextel™ 720 preform, repeated impregnation and pyrolysis of an alumina precursor, followed by oxidation of the carbon.³⁴ Preliminary results are presented in Fig. 6. With the fugitive coating, the composite exhibits significantly greater pullout as well as higher notched strength and fracture energy. The improvements are attributable to the combined effects of matrix porosity and the interfacial gap formed following carbon removal. The long-term stability and role of gap thickness in such systems is the focus of ongoing investigation.

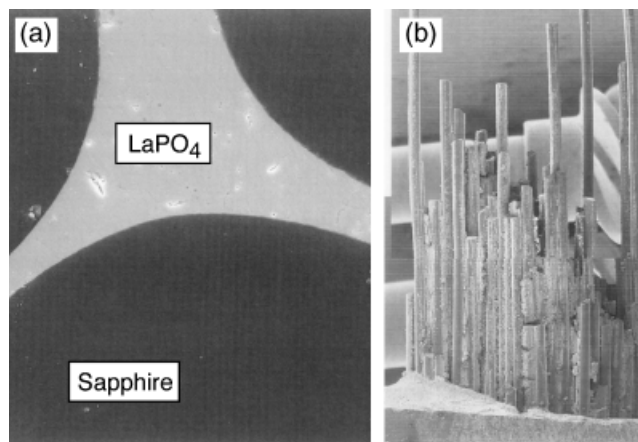


Fig. 4. (a) Microstructure and (b) fiber pullout in a dense LaPO₄ matrix reinforced with large-diameter sapphire fibers.³⁵ (Courtesy of Janet Davis, Rockwell Scientific. Reprinted from *J. Eur. Ceram. Soc.*, 19, J.B. Davis, D.B. Marshall, and P.E.D. Morgan, "Oxide Composites of Al₂O₃ and LaPO₄," pp. 2421-2426, 1999, with permission from Elsevier).

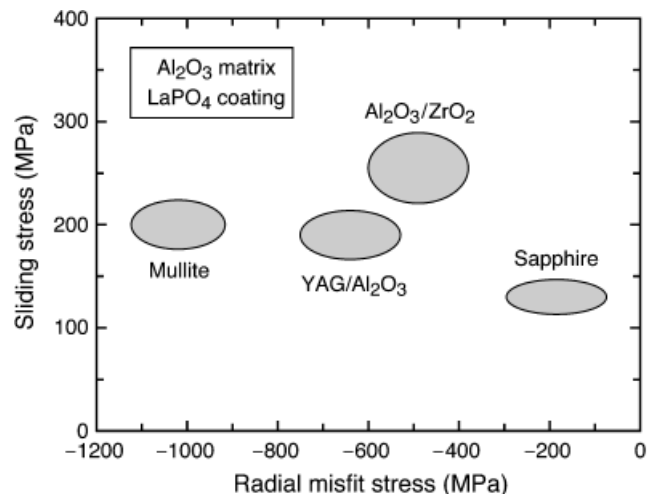


Fig. 5. Effects of radial misfit stress (from both thermal expansion mismatch and microstructural roughness) on the sliding stress of several monazite-coated fibers. (Adapted from Davis *et al.*²⁴).

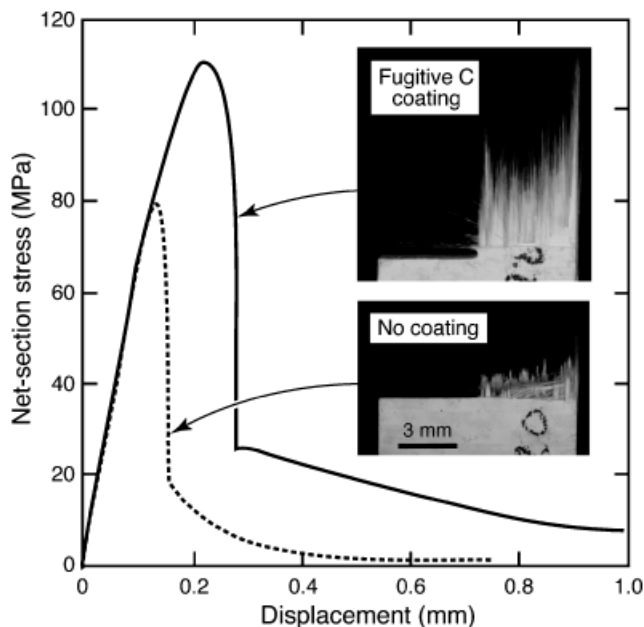


Fig. 6. Notched tensile behavior of a porous mullite-alumina matrix reinforced by Nextel™ 720 fibers, showing the effects of a fugitive carbon coating. (Courtesy J. H. Weaver).

(3) Hybrid Concepts

One approach that obviates the problems associated with weaving of coated tows and simplifies processing involves a hybridization of the coated-fiber and the porous-matrix schemes. Here, woven uncoated preforms are infiltrated with a monazite precursor solution containing fine alumina particles.³⁵ Following pyrolysis, a layer of monazite is formed on the fibers as well as between the alumina particles. The resulting matrix consists of a porous two-phase mixture of LaPO_4 and Al_2O_3 (Fig. 7(a)). The composite exhibits extremely large pullout lengths ($\gg 100R$, with R being the fiber radius; Fig. 7(b)) and virtually no detectable notch sensitivity in typical specimen configurations. These performance characteristics appear to be a consequence of (i) the monazite coating enabling crack deflection, and (ii) the low matrix stiffness reducing the radial constraints on the fiber, hence reducing the sliding resistance. (Contrary to other reports of fiber strength degradation following exposure to acidic precursors, the reported combination appears to be innocuous. It has been suggested that the alumina buffers the solution, making the fibers less susceptible to reaction with the precursors and the decomposition products formed during precursor pyrolysis).^{29,35}

In addition to the combined porous-matrix/coated fiber scheme, a second hybrid approach has emerged, using (in

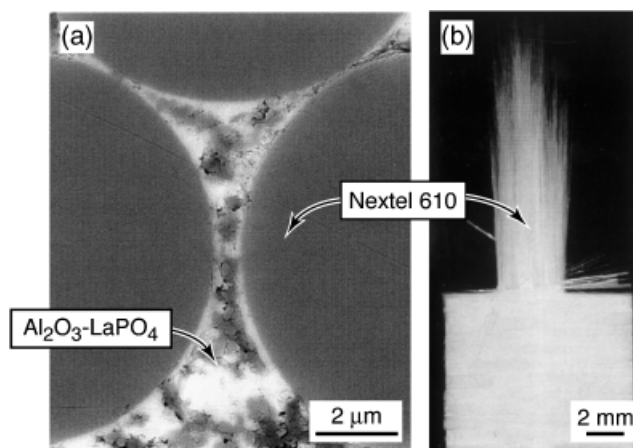


Fig. 7. (a) Microstructure and (b) fiber pullout in a porous $\text{LaPO}_4/\text{Al}_2\text{O}_3$ matrix reinforced with Nextel™ 610 alumina fibers. (Courtesy of Janet Davis, Rockwell Scientific. Reprinted from *J. Eur. Ceram. Soc.*, 19, J.B. Davis, D.B. Marshall, and P.E.D. Morgan, "Oxide Composites of Al_2O_3 and LaPO_4 ," pp. 2421–2426, 1999, with permission from Elsevier).

some sense) all three principal toughening schemes: porous matrices, fugitive coatings, and monazite coatings.³⁴ The initial processing steps are identical to those used to produce porous-matrix CFCCs with an interfacial gap (described above). Following oxidation of the carbon, a monazite precursor is repeatedly impregnated and pyrolyzed, thereby filling the interface gaps formerly occupied by carbon as well as between the matrix particles (Fig. 8). If successful, this approach could provide an effective route to fabricating coated fiber composites with virtually any architecture and configuration. A critical assessment of performance and durability of this class of composite has yet to be made.

III. Matrix-Enabled Damage Tolerance

(1) Microstructural Concept

When introduced in the mid-1990s,^{5–8} the porous-matrix concept was motivated principally by two factors: (i) the lack of a suitable suite of coatings for oxide fibers, and (ii) the expectation of reduced manufacturing costs resulting from the absence of coatings. Although the concept has proven to be an effective alternative to fiber coatings for enabling damage tolerance, it has several inherent limitations: (i) CFCCs with two-dimensional (2D) fiber architectures exhibit low thermal conductivity, strength, and fracture resistance in the through-thickness direction; (ii) regardless of fiber architecture, these composites are non-hermetic; (iii) they are expected to have lower compressive strengths than the dense matrix counterparts, because of the reduced constraint on fiber microbuckling; and (iv) they are more susceptible to wear.³⁶

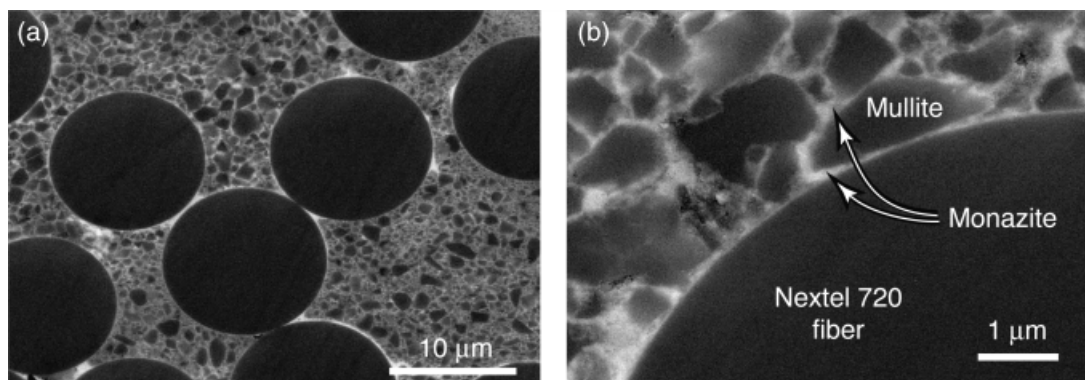


Fig. 8. Scanning electron micrographs of an oxide continuous-fiber ceramic composite (using backscatter electron imaging). Monazite is present within the interface gap produced by removal of the fugitive carbon as well as between matrix particles. (Monazite precursor provided by Janet Davis, Rockwell Scientific).

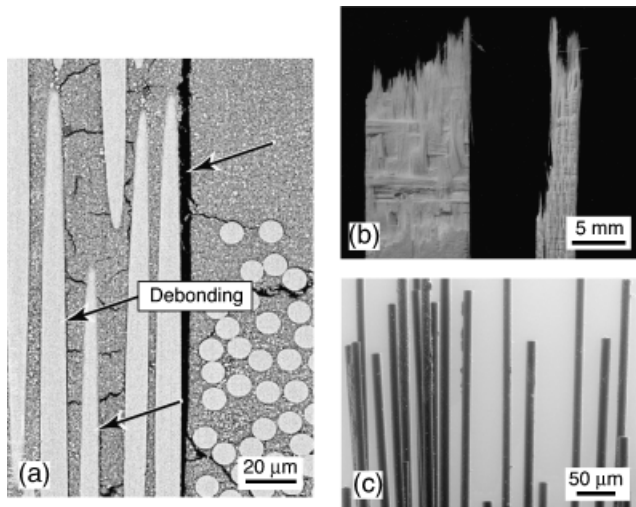


Fig. 9. Damage and fracture mechanisms in a porous-matrix oxide continuous-fiber ceramic composite. (a) Crack deflection and interface debonding in a notched bend specimen. The specimen was infiltrated with epoxy while under load and then sectioned and polished. (b, c) Uncorrelated fiber failure and pullout. Material consists of Nextel™ 720 fibers in an eight-harness satin weave and a mullite–alumina matrix.

To ensure a morphologically stable pore structure, the matrices typically consist of two dissimilar phases, distinguished by their sintering kinetics. The major phase is present as a contiguous 3D particle network. In turn, the network is bonded by a less refractory ceramic or glass binder, in the form of either smaller sinterable particles or the product of precursor pyrolysis. Particles in the main network dictate the long-term stability of the matrix against sintering, whereas particle junctions formed by the binder control the mechanical integrity of the matrix. Additionally, the junctions at the fiber surface control the interfacial toughness.

When properly implemented, porous-matrix CFCCs exhibit fracture characteristics similar to those of conventional dense-

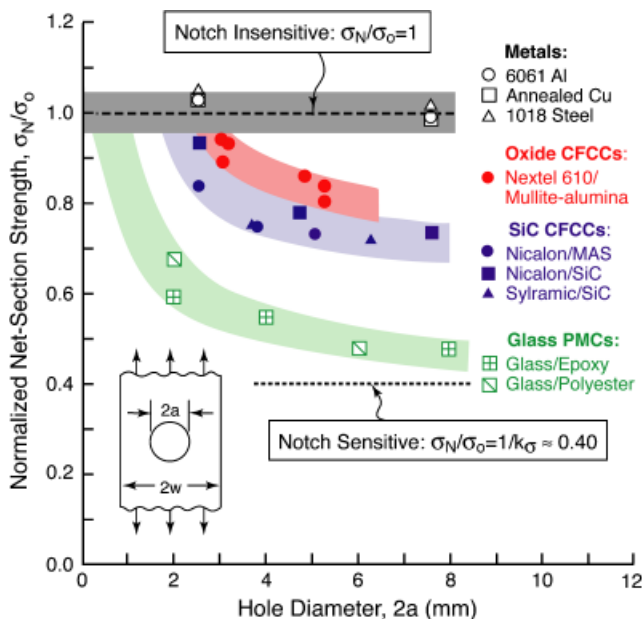


Fig. 10. Open-hole tensile strength of metals, oxide, and SiC continuous-fiber ceramic composites (CFCCs), and polymer matrix composites. σ_0 is the unnotched tensile strength and $k\sigma$ is the elastic stress concentration factor. All composites have two-dimensional fiber architectures (either laminated or woven) and loads are applied parallel to one of the fiber axes. The normalized hole diameter is $a/w = 0.2$ for all cases except the oxide CFCC, wherein $a/w = 1/3$.

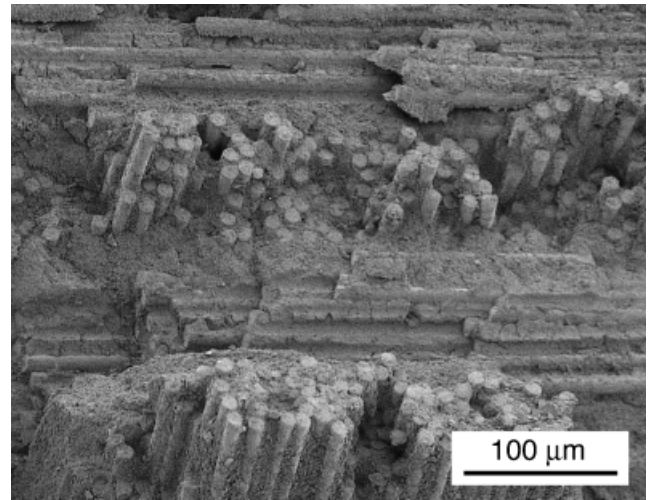


Fig. 11. Minimal fiber pullout on the fracture surface of a mullite-based porous matrix continuous-fiber ceramic composite strengthened with an excessive amount of a precursor-derived alumina. (Courtesy M. A. Mattoni).

matrix, coated-fiber systems. That is, matrix cracks deflect along the fiber–matrix interface and fibers subsequently fail in an uncorrelated manner, leading to pullout (Fig. 9). Additionally, the degree of notch sensitivity, characterized by open hole tension tests, is comparable in the two classes of materials (Fig. 10).⁹ In contrast, when the matrix is sintered or densified excessively, either through processing or subsequent elevated temperature (in-service) exposure, embrittlement ensues. This is manifested in planar fracture surfaces with minimal fiber pullout and significantly reduced toughness (Fig. 11).

(2) Debonding Mechanics

The role of matrix porosity in enabling damage tolerance is twofold. Firstly, the bond between the matrix and the fibers is inherently weak. That is, the interface toughness, Γ_i , can be no greater than that of the matrix itself; for typical porosity levels ($\sim 30\%$), the matrix toughness, Γ_m , is about an order of magnitude lower than that of the fibers, Γ_f , thereby ensuring a low-toughness interface. Secondly, because energy release rates scale with elastic moduli, the reduction in modulus due to porosity leads to a reduction in the driving force for matrix cracks.

To achieve high toughness in CFCCs, matrix cracks must deflect into the fiber/matrix interface rather than penetrate into the fibers. (A second condition—that interface sliding occur with only moderate resistance—must also be satisfied.) The conditions that satisfy this requirement are plotted in Fig. 12(a).³⁷ Deflection is predicted when the toughness ratio, Γ_i/Γ_f , is less than the energy release rate ratio, G_d/G_p , associated with deflection and penetration. The latter is a function of the elastic mismatch parameter,

$$\Delta \equiv \frac{(\bar{E}_f - \bar{E}_m)}{(\bar{E}_f + \bar{E}_m)} \quad (1)$$

where \bar{E} is the plane strain modulus, and the subscripts f and m denote fiber and matrix, respectively. For porous-matrix systems, Δ takes on high values (> 0.5); hence, the allowable toughness ratio is also high.

Because of similarities in the matrix and fiber constituents in oxide CFCCs of present interest, the nature of bonding at the fiber–matrix interface is similar to that between particles in the matrix. Consequently, their toughnesses are expected to move in tandem: that is, $\Gamma_i = \omega\Gamma_m$ where ω is a non-dimensional parameter. As the packing density of matrix particles at the fiber surface is lower than that in the bulk,³⁸ $\Gamma_i < \Gamma_m$ and hence $\omega < 1$. For conservative design, ω is taken to be 1.

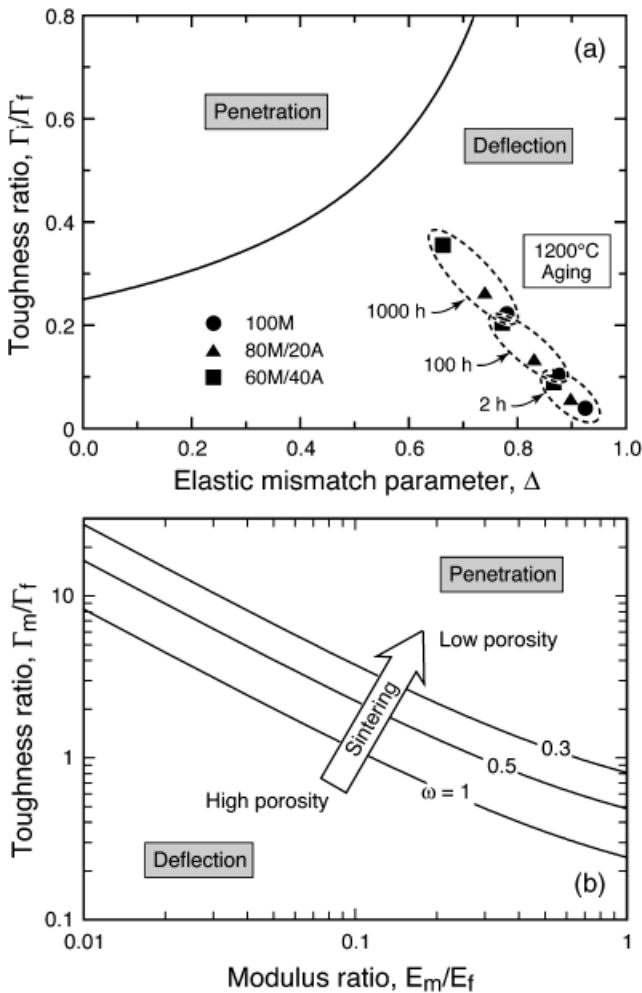


Fig. 12. (a) Conditions for crack deflection at a fiber–matrix interface (adapted from He and Hutchinson³⁷). Experimental data are for mullite–alumina particle mixtures, assuming a toughness ratio $\omega \equiv \Gamma_i/\Gamma_m = 1$ and fiber properties $\Gamma_f = 15 \text{ J/m}^2$ and $E_f = 260 \text{ GPa}$. (b) Complementary representation of crack deflection conditions, showing the critical combination of matrix toughness and modulus as well as the effects of ω .

An estimate of the property combination that leads to deflection is obtained in the following way. For $\Delta \geq 0$, the energy release rate ratio is well described by the empirical equation

$$\frac{G_d}{G_p} = \frac{1}{4(1 - \Delta)^{0.9}} \quad (2)$$

This formula has an error $\leq 4\%$ over the range $0 \leq \Delta \leq 0.95$. Upon setting $G_d/G_p = \Gamma_i/\Gamma_f$ and combining the result with Eq. (1), the deflection condition can be re-expressed as¹

$$\Sigma \equiv 0.13 \left(\frac{\Gamma_f}{\Gamma_m} \right) \left(1 + \frac{E_f}{E_m} \right)^{0.9} > \omega \quad (3)$$

where Σ is a non-dimensional parameter that characterizes the propensity for crack deflection.

The requisite combinations of Γ_m/Γ_f and E_m/E_f are plotted in Fig. 12(b) for three assumed values of ω (0.3–1). As matrix sintering/densification proceeds, the properties follow a trajectory from the lower left corner of the diagram (when the porosity is high) to the upper right, eventually crossing the boundary

between deflection and penetration. Pertinent experimental measurements and modeling studies on the matrix properties Γ_m and E_m are presented in Section V. Upon combining with the corresponding fiber properties via Eq. (3), an assessment is made of the efficacy of the porous-matrix concept for a specific matrix/fiber combination (Section V(4)).

IV. Evolution of Porous-Matrix Materials

Early generations of porous-matrix CFCCs (produced by General Electric (Cincinnati, OH) and later by COI Ceramics (San Diego, CA)) comprise alumina powder and a silica-forming polymer precursor.⁶ Commercially, the composites are manufactured using procedures adapted from the polymer composites industry. Prepregs are made by immersing woven fiber cloth into a dispersed ceramic slurry. They are then stacked, warm molded in an autoclave, and fired at an elevated temperature (typically 1000°C) to remove organics and pyrolyze the polymer. This process yields a contiguous nanoporous silica phase within an alumina particle network. Although the early generation composites with these constituents exhibited attractive mechanical properties after fabrication, significant degradation was obtained following extended heat treatments at temperatures beyond 1000°C: a consequence of matrix sintering. A variant of this concept uses a precursor-derived alumina as the binder (in place of silica), with the intent of enhancing morphological stability. However, the alumina particle network remains susceptible to densification at yet higher temperatures (1100°–1200°C), typical of targeted service conditions, especially when the particles are fine ($< 1 \mu\text{m}$).

More significant enhancements in stability have been achieved through the use of mullite as the main matrix constituent and alumina as the binder.^{8,12} In a common implementation, mullite powder is dispersed in an aqueous slurry and infiltrated into a fiber preform via a vacuum-assisted technique. The alumina is introduced in one of two ways: by mixing fine alumina particles into the mullite-containing slurry, or by subsequent impregnation and pyrolysis of an alumina precursor solution.³⁹ The two processing routes lead to distinctly different matrix topologies, shown schematically in Fig. 13(a). Compositional maps of two prototypical systems are presented in Fig. 13(b).^{40,41}

The preceding processing routes and the resulting microstructures are characterized by three attributes:

(i) The mixed mullite/alumina slurry method allows both matrix phases to be infiltrated simultaneously. By contrast, the precursor route requires additional steps, beyond that of slurry infiltration, and is thus more costly.

(ii) The presence of particulate alumina can compromise the stability of the mullite network, especially if its proportion exceeds the percolation threshold.⁴² Conversely, if the slurry is comprised of only mullite and the alumina is introduced subsequently via the precursor route, the contiguity of the mullite network is ensured.

(iii) Because of limitations on the allowable fraction of particulate alumina (to inhibit densification), the slurry route results in matrices that are relatively weak. Although essential for crack deflection, this weakness compromises the off-axis properties, especially the resistance to delamination. In contrast, the precursor route allows for filling of the void space between the particles in the network (at least while the pores remain open), resulting in increases in the mechanical integrity of the network. The latter route provides access to a broader range of matrix properties.

The morphological stability of porous mullite–alumina matrices at the targeted upper use temperatures of oxide CFCCs has been demonstrated through experiments on neat (fiber-free) materials (Fig. 14(a)).⁴² Specifically, compacts of $1 \mu\text{m}$ mullite particles exhibit no detectable shrinkage after 1000 h of exposure at 1200°C. Mixtures containing $\leq 20\%$ alumina particles ($0.2 \mu\text{m}$ diameter) are similarly stable, with porosity changing $< 0.5\%$

¹Here, Poisson's ratios of the fiber and the matrix are assumed to be the same. Consequently, the plane strain modulus ratio \bar{E}_f/\bar{E}_m can be replaced with the Young's modulus ratio E_f/E_m .

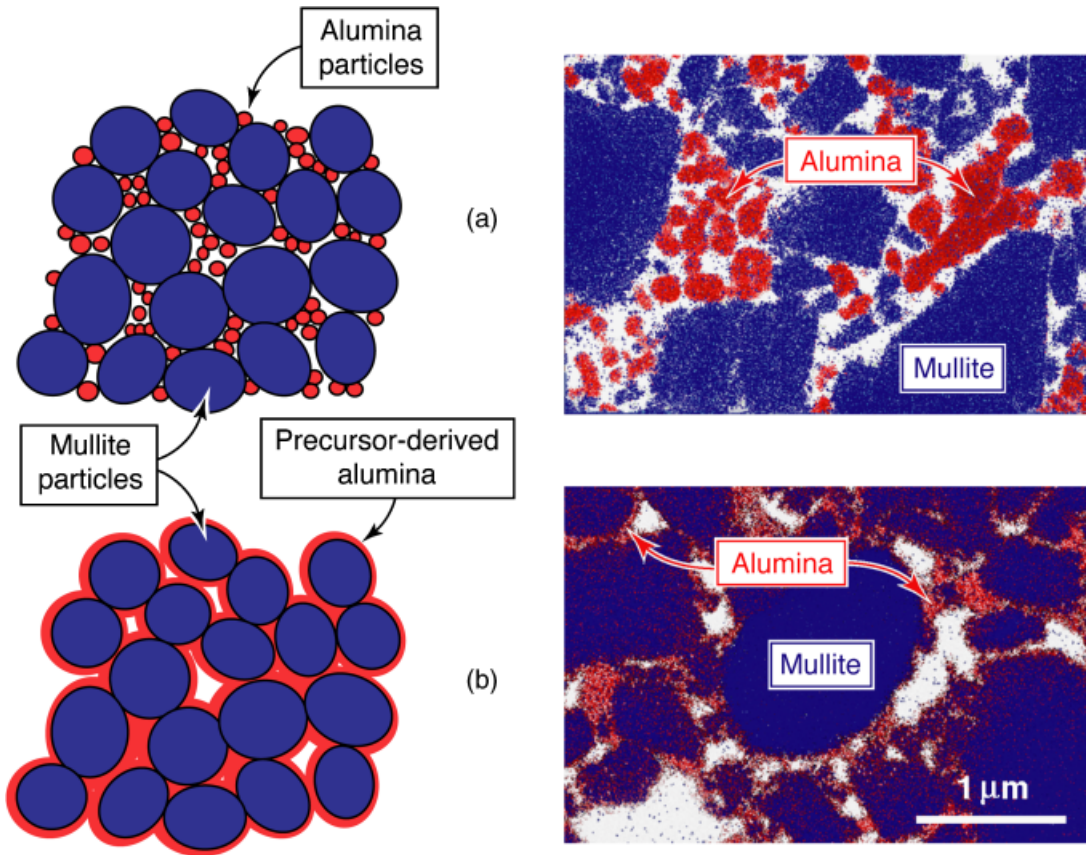


Fig. 13. (a) Schematics of the matrix topologies produced by mullite/alumina particle mixtures (top) and mullite particles bonded by precursor-derived alumina (bottom). (b) Compositional maps produced by energy-dispersive spectroscopy of TEM foils. The top image shows a particle mixture of 80% mullite and 20% alumina (without precursor addition), whereas the bottom one is of a mullite powder compact bonded by 15% precursor-derived alumina. (Adapted from Fujita *et al.*⁴⁰).

during the same aging cycle. Some shrinkage occurs for higher alumina content ($\geq 30\%$), but its evolution remains extremely sluggish in relation to that for pure alumina powder (inset in Fig. 14(a)), by about four orders of magnitude. The results confirm that the mullite network is effective in inhibiting matrix densification, even for relatively large amounts of the sinterable phase.

Despite the absence of shrinkage, both Young's modulus E and the toughness Γ increase appreciably with aging time, by a factor of 3–4 (Fig. 14(b)): a consequence of surface-diffusion-controlled sintering at the particle junctions.⁴² The implications for crack deflection are addressed in a subsequent section.

Yet further enhancements in matrix properties have been achieved through the design of *all-mullite* matrices.⁴³ The concept uses two particle populations with vastly dissimilar sizes (e.g., 1 and 0.1 μm) and exploits the differences in their sintering kinetics. When present in the appropriate proportion, the smaller particles can be readily sintered to the larger particles without compromising the stability of the main network. In principle, a similar structure could be achieved using mullite precursor solutions. However, the temperatures required for mullitization are well beyond those that the present fibers can withstand without degradation.

An additional processing enhancement involves use of a time-delayed setting agent (e.g., AlN) in the slurry.⁴³ The agent

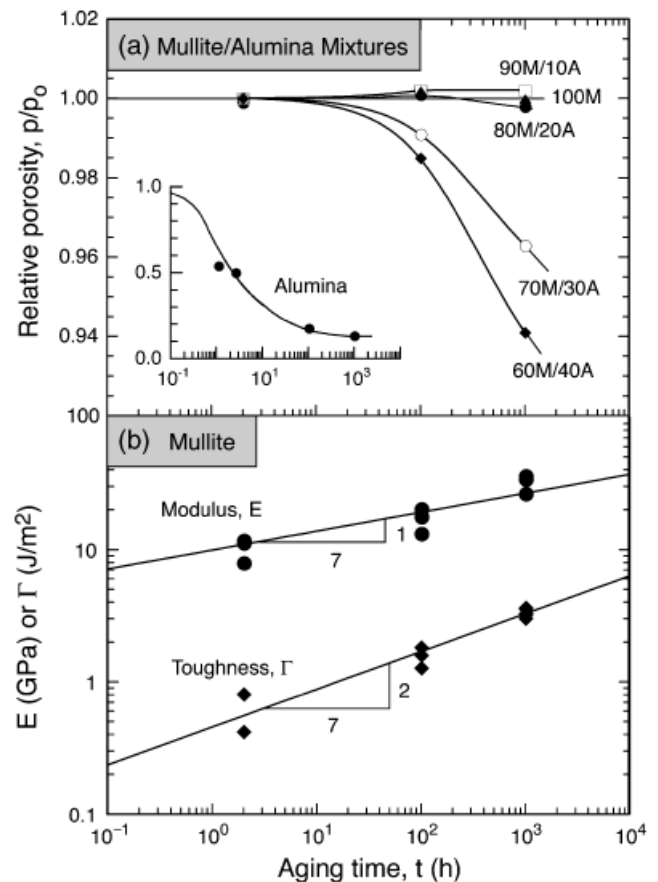


Fig. 14. (a) Effects of aging at 1200°C on the porosity of mixed mullite–alumina compacts with compositions ranging from 100% mullite (denoted 100M) to 60% mullite and 40% alumina (60M/40A). (b) Corresponding property changes of pure mullite. Sintering occurs by a surface diffusion mechanism with diffusivity $\delta_s D_s = 4 \times 10^{-30} \text{ m}^3/\text{s}$. The inferred junction toughness is $\Gamma_j \approx 3 \text{ J/m}^2$; only slightly higher than the surface energy contribution ($2\gamma \approx 2 \text{ J/m}^2$).

produces a gradual increase in pH and a corresponding reduction in the ζ potential between particles. Upon reaching the isoelectric point, the slurry coagulates. The process is designed to affect coagulation after completion of vacuum bagging such that the green preform exhibits substantially increased mechanical integrity for subsequent handling.

V. Properties of Porous Matrices

Significant progress has been made in the understanding of the mechanical properties of porous matrices and their dependence on the topology of the constituent phases as well as their evolution with time. The key results from analytical models, numerical simulations, and experimental measurements are presented below.

(1) Monophase Particle Networks

Junction growth due to sintering in a monophase particle network follows a power law of the form^{44,45}:

$$\frac{a}{R} = \left(\frac{t}{t_R}\right)^{1/n} \quad (4)$$

where a is the junction radius, R is the particle radius, t is the sintering time, t_R is a reference time, and n is a constant; both t_R

and n depend on the transport mechanism ($n = 3$ for vapor transport, $n = 5$ for lattice diffusion, and $n = 7$ for surface diffusion). Provided $a/R \ll 1$, Young's modulus of the bonded aggregate scales linearly with junction radius in accordance with^{46,47}

$$\frac{E}{E_p} = \zeta \left(\frac{zD}{2\pi}\right) \left(\frac{a}{R}\right) \quad (5)$$

where E_p is Young's modulus of the particles; z is the particle coordination number (approximately six for random packing); D is the relative packing density; and $\zeta \approx 0.76$ (calculated by the discrete element method (DEM), described in Sidebar A). Combining Eqs. (4) and (5) yields the time dependence of the modulus

$$\frac{E}{E_p} = 0.76 \left(\frac{zD}{2\pi}\right) \left(\frac{t}{t_R}\right)^{1/n} \quad (6)$$

When sintering occurs by surface diffusion ($n = 7$), the time dependence is weak: a 10-fold increase in time leads to a modulus increase of only 10%. This has important consequences on the long-term durability of mullite-based CFCCs under typical service conditions.

The relationship between toughness and junction radius for a bonded particle aggregate has been obtained from numerical

Sidebar A. Numerical Simulation of Bonded Particle Aggregates

Young's modulus of a bonded particle aggregate is simulated numerically using the discrete element method (DEM).⁴⁷ The junction response that defines the element properties is derived from finite element analysis (FEA) of a single particle in a periodic array. The interaction between particle junctions, characterized by the displacement of one junction due to the force acting on another, is also derived from FEA. An isotropic random aggregate of touching spherical particles is then generated using a computer algorithm (inset of Fig. A1(a)). To ensure equilibrium, each particle is required to touch at least three neighbors upon placement onto the aggregate. The final particle packing density is 55% and the average coordination number is 6: consistent with measured values for random loose packing of spherical particles.

For monophase systems, junction growth is simulated by uniformly expanding the particles and re-distributing the overlapping material uniformly over the free surface of the particles. In contrast, for systems containing a precursor-derived binder, the material is modeled as an aggregate of touching monophase particles, each coated with a uniform layer of the second phase. The elastic response of the junctions is calculated by FEA of a periodic array with the two phases explicitly discretized. For both mono- and two-phase systems, the particle network is then subjected to a prescribed macroscopically uniform strain field and the effective elastic response is determined using DEM. Typical numerical results and comparisons with experimental measurements⁴⁸ are shown in Fig. A1(a).

The toughness of the aggregate is also computed by DEM (Fig. A1(b)).⁴² In this case, a crack is defined by a plane separating particles that have had the junctions between them broken (inset of Fig. A1(b)). The simulation proceeds by incrementally increasing the remote displacement (for tension) or the remote rotation (for bending), while allowing the junctions at the crack tip to fail at a critical junction stress, σ_c , given by:

$$\sigma_c = 2\sqrt{\frac{E_p \Gamma_j}{\pi a}}$$

where Γ_j is the junction toughness. The results of the simulations (Fig. A1(b)) are well described by Eq. (7) in the text.

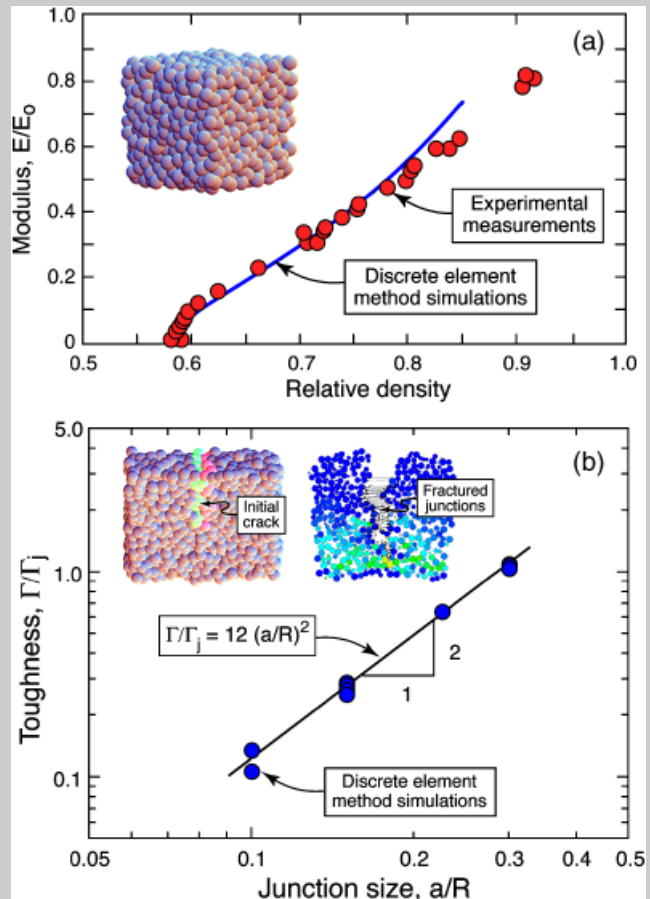


Fig. A1. Discrete element method simulations of (a) Young's modulus and (b) toughness of monophase-bonded particle aggregates. Experimental measurements in (a) are for alumina (from Green *et al.*⁴⁸).

simulations of fracture using the DEM (Sidebar A).⁴⁹ The results of the simulations are well described by

$$\frac{\Gamma}{\Gamma_j} = 12 \left(\frac{a}{R} \right)^2 \quad (7)$$

where Γ_j is the junction toughness. (The scaling with a^2 is a consequence of the dependence of toughness on junction area.) Combining Eqs. (4) and (7) yields the corresponding time dependence

$$\frac{\Gamma}{\Gamma_j} = 12 \left(\frac{t}{t_R} \right)^{2/n} \quad (8)$$

Although this sensitivity is greater than that of the modulus, the magnitude of the effect is small when surface diffusion is the operative sintering mechanism.

An assessment of these models is made through comparison with measurements on pure mullite compacts (Fig. 14(b)).⁴² Consistent power-law scalings of modulus and toughness with time are obtained for aging times up to 10^3 h. Furthermore, upon extrapolation, the modulus and the toughness are predicted to increase by only 10% and 20%, respectively, for an additional 10^4 h of exposure at 1200°C (typical of turbine engine components). Such extrapolations are used in estimating long-term durability of oxide CFCCs, demonstrated below.

(2) Two-Phase Particle Networks

The preceding models for junction growth and property changes in monophase aggregates are extended to two-phase particle mixtures (such as those comprising porous matrices in CFCCs).⁴² For a generic mixture of A and B particles, three junction types are present: A–A, A–B, and B–B. The aggregate properties are obtained by averaging the junction properties, weighted by the number fraction of the associated junction type. To facilitate tractable solutions, the two particle types are assumed to be the same size and arranged randomly in the mixture. A statistical analysis yields the junction fractions, f

$$f_{AA} = X_A^2 \quad (9a)$$

$$f_{BB} = (1 - X_A)^2 \quad (9b)$$

$$f_{AB} = 2X_A(1 - X_A) \quad (9c)$$

where X_A is the number fraction of A particles.

Young's modulus of the two-phase mixture is modeled following an approach similar to that used for monophase systems,⁴⁶ with appropriate modifications to reflect differences in junction characteristics. (i) The description of junction stiffness is modified to account for the moduli of the particles on either side of the junction. In the Hertzian limit, the stiffness of dissimilar particle junctions is proportional to $2\lambda/(1+\lambda)$ where $\lambda \equiv E_A/E_B$.⁴⁹ (ii) The area of the A–B junction is assumed to be the average of the areas of the A–A and B–B junctions. This result is expressed in non-dimensional form as $a_{AB}/a_{BB} = \sqrt{(1+\eta)/2}$ where η is a junction area ratio, defined by $\eta \equiv (a_{AA}/a_{BB})^2$. (iii) The modulus is determined from the arithmetic mean of junction stiffness, weighted by the respective number fractions, given by Eq. (9). The result is:

$$\frac{E}{E_B} = X_A^2 \lambda \sqrt{\eta} + 2X_A(1 - X_A) \sqrt{\frac{(1+\eta)}{2}} \left(\frac{2\lambda}{1+\lambda} \right) + (1 - X_A)^2 \quad (10)$$

Upon comparing with numerical simulations, this result is found to be accurate in the domain in which the sinterable phase comprises $\leq 40\%$ of the total.

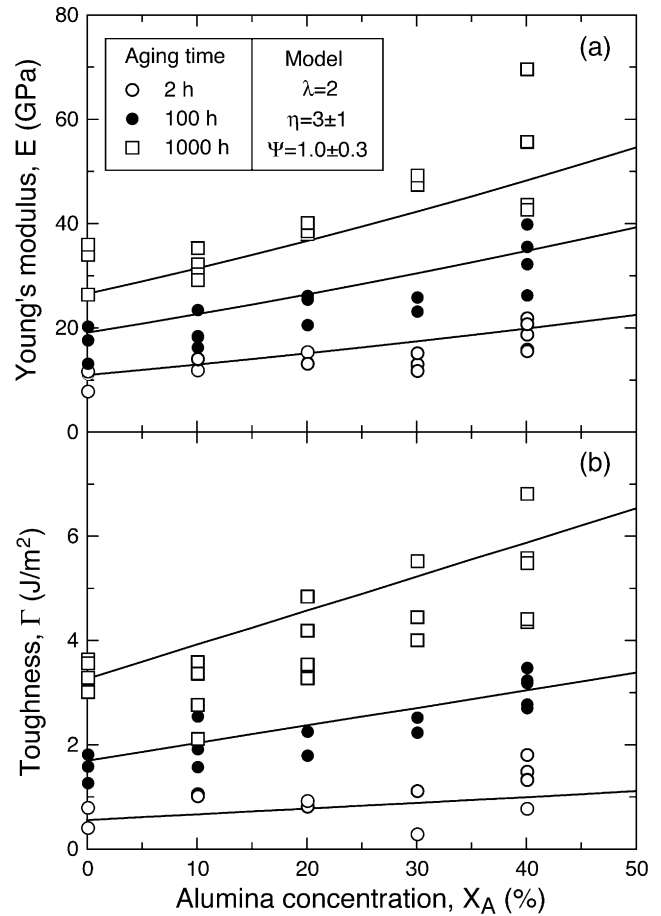


Fig. 15. Effects of composition and aging time on (a) Young's modulus and (b) toughness. The solid lines represents model predictions (Eqs. (10) and (11)). Adapted from Fujita *et al.*⁴²

An analogous model for the toughness of a mixed aggregate is obtained when the contribution from each junction type is assumed to be proportional to $\Gamma_j(a/R)^2$ and the toughnesses of the different types of junctions are then weighted by their respective number fractions Eq. (9). The result is

$$\frac{\Gamma}{\Gamma_M} = X_A^2 \Psi \eta + 2X_A(1 - X_A) \left(\frac{1+\eta}{2} \right) \left(\frac{1+\Psi}{2} \right) + (1 - X_A)^2 \quad (11)$$

where Γ_{AA} , Γ_{BB} , and Γ_{AB} are the junction toughnesses; $\Psi \equiv \Gamma_{AA}/\Gamma_{MM}$; and Γ_{AB} is taken to be the average of Γ_{AA} and Γ_{BB} .

The models are assessed by comparison with experimental measurements on the mullite/alumina system, for which $\lambda = 2$ (Fig. 15).⁴² The unknown parameters are η and Ψ . Fitting the modulus measurements yields a junction area ratio $\eta \approx 3 \pm 1$: consistent with the expectation that the alumina-containing junctions should sinter more rapidly than those with only mullite. Then, upon fitting the toughness measurements, the inferred toughness ratio is $\Psi = 1.0 \pm 0.3$. The implications are twofold: (i) the toughnesses of the three junction types are similar to one another, and (ii) the increase in aggregate toughness with alumina content is due largely to the increase in the average junction area.

(3) Precursor-Derived Two-Phase Networks

When the binder phase is produced by a precursor route, the resulting topology is markedly different. For modeling purposes, the topology is represented by one of two limiting idealizations. In both, the major phase is treated as a contiguous network of uniform particles, radius R , and with average

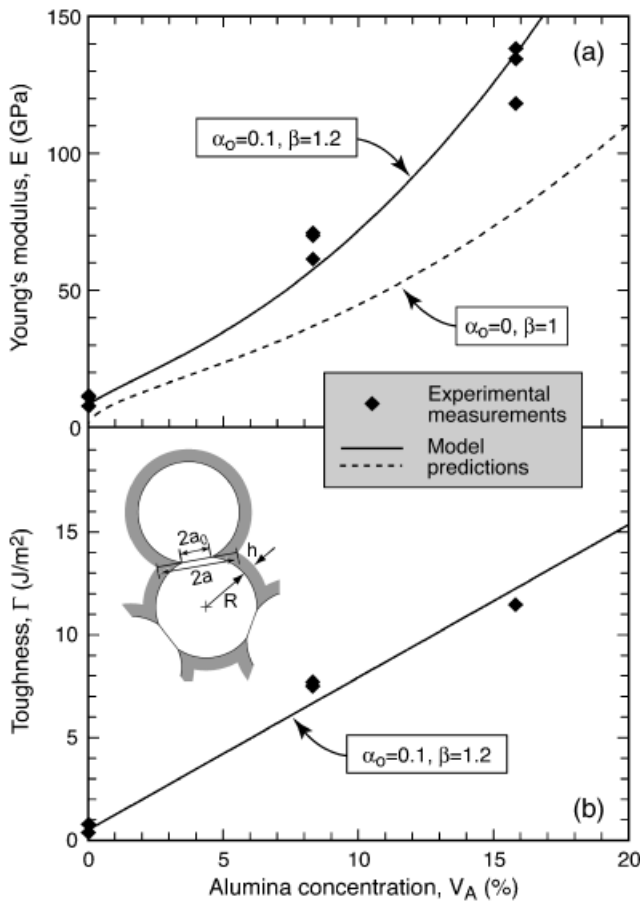


Fig. 16. Summary of measurements and model predictions of (a) Young's modulus and (b) toughness. The material is made of a mullite particle network, strengthened by precursor-derived alumina. (Adapted from Fujita *et al.*⁴⁰).

junction radius, a_0 . In one limit, the binder phase is a porous homogeneous continuum occupying all available space in the interstices of the particle network. This idealization is applicable to the as-processed aluminosilicate matrices, wherein the silica glass exists as a contiguous nanoporous phase within the alumina particle network. In the other, the binder is modeled as a uniform coating, thickness h , on the particle surfaces (inset of Fig. 16). This is the preferred representation for the mullite–alumina system (Fig. 13) and forms the basis for the ensuing analysis.

From geometry, the normalized net junction radius α is given by⁴⁰

$$\alpha \equiv \frac{a}{R+h} \approx \sqrt{\frac{2\beta^2 V_B}{3(1-p_0)}} + \alpha_0^2 \quad (12)$$

where $1-p_0$ is the volume fraction of the particulate phase; V_B is the volumetric concentration of the precursor-derived binder; $\alpha_0 \equiv \alpha_0/(R+h)$; and β is a non-dimensional parameter that accounts for preferential binder accumulation at the particle junctions ($\beta = 1$ for uniform coatings). For the case in which the elastic properties of the two phases are the same, computer simulations based on the DEM of Young's modulus are accurately described by the empirical equation

$$\frac{E}{E_P} = 0.4\alpha(1 + 14\alpha^3) \quad (13)$$

where E_P is the modulus of the solid particles. More generally, when the properties of the two phases differ, the modulus of the two-phase aggregate is estimated from the weighted average of the moduli of the two monophase aggregates, evaluated at

the same value of α . Operationally, this estimate is obtained by replacing E_P in Eq. (13) with the volume-weighted average of the moduli of the two solid phases, yielding the result

$$E = 0.4\alpha(1 + 14\alpha^3)[E_P v_P + E_B(1 - v_B)] \quad (14)$$

where

$$v_P = \frac{1 - p_0}{1 - p_0 + V_B} \quad (15)$$

and E_B is the modulus of the binder. Upon combining Eqs. (13)–(15), the estimated modulus of the two-phase system becomes:

$$\frac{E}{E_P} = 0.4\alpha(1 + 14\alpha^3) \left[\frac{(1 - p_0) + (E_B/E_P)V_B}{(1 - p_0) + V_B} \right] \quad (16)$$

An analogous approach yields estimates of toughness. When the properties of the two phases are the same, the results from DEM simulations (Sidebar A) are well described by

$$\frac{\Gamma}{\Gamma_j} = 12\alpha^2 \quad (17)$$

When adapted to the general case in which the properties of the two phases differ, the toughness becomes

$$\frac{\Gamma}{\Gamma_j} = 12 \left(\beta^2 \frac{2V_B}{3(1-p_0)} + \alpha_0^2 \right) \quad (18)$$

Comparisons between the model predictions and the experimental measurements for the mullite–alumina system are plotted in Fig. 16. When the parameters are selected to be $\beta = 1.2$ and $a_0/R = 0.1$, the model provides a good fit to the modulus data. In contrast, when they are taken as $\beta = 1$ and $a_0/R = 0$, the modulus of the pure mullite is erroneously predicted to be 0 and the rate of increase with volume fraction is underestimated. For consistency, the same (former) values of β and a_0/R are used for modeling the toughness, with Γ_j the only unknown parameter. Upon fitting the data (Fig. 16), the junction toughness is inferred to be $\Gamma_j = 4 \text{ J/m}^2$: only slightly greater than that of pure mullite ($\Gamma_j = 3 \text{ J/m}^2$).

(4) Implications for Crack Deflection

Once calibrated, the preceding models are coupled with the analysis in Section III to assess the propensity for crack deflection, as manifest in the parameter Σ . The results are plotted in Fig. 17(a) for mullite–alumina particle mixtures combined with Nextel™ 720 fibers. In this case, crack deflection is predicted over the entire range of compositions (0%–40% alumina) and aging times (to 1000 h). As a complementary representation, a subset of these results is plotted in Fig. 12(a) (assuming $\omega = 1$). Here, again, the property combinations lie within the crack deflection domain. Moreover, the interface sliding stress in these systems is low, typically $< 10 \text{ MPa}$ (Sidebar B), re-affirming that mullite–alumina mixtures are good candidates for use in oxide composites.

The critical aging time t_c for crack penetration is obtained by extrapolating the predictions in Fig. 17(a) to $\Sigma = \omega = 1$. It ranges from 4000 h for mixtures of 60% mullite–40% alumina to 60 000 h for pure mullite, the latter being comparable with the targeted service lives of CFCC components. With knowledge of the activation energy of the sintering mechanism, the model can be readily extended to other temperatures.

A similar assessment is made of the mullite particle networks strengthened by precursor-derived alumina, again assuming the re-inforcements to be Nextel™ 720 fibers. The results are plotted in Fig. 17(b). Here, Σ decreases with increasing alumina concentration, V_A , and eventually falls below the critical value, $\omega \approx 1$, at $V_A \approx 9\%$. This point is expected to mark the onset of crack penetration into the fibers and a significant loss in damage tolerance.

Sidebar B. Fiber Push-In Testing of Porous Matrix CFCCs

The interfacial debonding and sliding properties are most conveniently probed by fiber push-in testing.⁵⁰ The test is performed using an instrumented indenter, usually with a sharp diamond tip (Berkovich or Vickers), resulting in plastic deformation of the fiber beneath the tip. To ascertain the sliding displacement from the measured (total) value, the plastic displacement associated with fiber yielding must be measured on a reference (non-sliding) fiber. Typically, the reference state is produced by fabricating a composite without a fiber coating and subjecting it to a heat treatment that produces strong interfacial bonds.

As porous-matrix CFCCs do not rely on fiber coatings, the usual technique for producing a reference fiber is impractical. Furthermore, because of its low stiffness, the matrix surrounding the pushed fiber undergoes an indeterminate amount of elastic displacement during fiber push-in, concurrent with plastic displacement of the fiber surface and sliding along the interface. Consequently, if the reference fibers were embedded in a *dense* matrix, the test results would not capture all of the extraneous displacement.

In light of these problems, a variant on the established push-in technique has been developed for use with porous matrix CFCCs.⁵¹ Two changes have been implemented: (i) a blunt (spheroconical) indenter that produces *only elastic* deformation is used for fiber pushing; and (ii) the hysteresis loop width is used for analysis, rather than the absolute displacement. The loop width is obtained by subtracting the *measured* displacements on loading and unloading at each load level; as all extraneous displacement is elastic, it does not contribute to the displacement difference.

A full analysis of the hysteresis loops is presented in Weaver *et al.*⁵¹ The pertinent solutions are summarized in Table BI. Representative measurements for a system with a particulate mullite–alumina matrix are in Fig. B1.

Table BI. Solutions for Fiber-Push-in Test

| Definitions | |
|---|---|
| E_f —fiber modulus | $\Delta_* \equiv \frac{F_M^2}{4\pi^2 R^3 \tau E_f}$ |
| F_C —critical force for debond initiation | $\gamma \equiv \frac{4\pi^2 \Gamma R^3 E_f}{F_M^2}$ |
| F_M —maximum force | $k \equiv \frac{F}{F_M}$ |
| R —fiber radius | $F_C = 2\pi\sqrt{R^3 E_f \Gamma}$ |
| τ —sliding stress | |
| Γ —debond energy | |
| Loop Width | |
| Cycle 1 | Cycle 2 |
| $\frac{\Delta_1}{\Delta_*} = (1 - \gamma) \left(1 - \frac{1}{2}(1 - k)^2\right)$ ($0 \leq F \leq F_C$) | $\frac{\Delta_2}{\Delta_*} = k(1 - k)$ ($0 \leq F \leq F_M$) |
| $\frac{\Delta_1}{\Delta_*} = \frac{1}{2} + k - \frac{3k^2}{2}$ ($0 \leq F \leq F_C$) | |

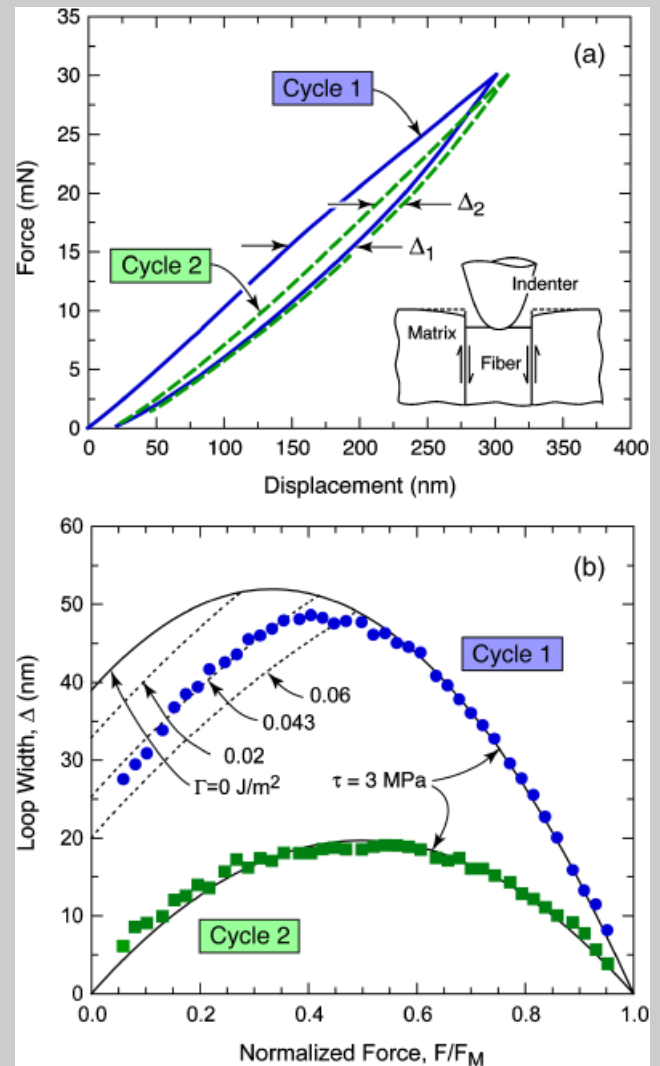


Fig. B1. (a) Force–displacement curves from a fiber push-in test on a porous mullite–alumina matrix continuous-fiber ceramic composite.⁵¹ The inset shows the test configuration. (b) Loop width measurements along with analysis to ascertain debond energy and sliding stress. (F_M is the maximum force in the test).

VI. Thermomechanical Stability of Porous-Matrix CFCCs

The stability of the pore structure in a CFCC without fiber coatings is vital to composite durability. A useful metric for assessment of stability is the strength retention following extended high-temperature exposure. The results of this type for three families of porous-matrix CFCCs following 1000-h exposures are plotted in Fig. 18(a). All are reinforced with Nextel™ 720 fibers in an eight-harness satin weave. They are distinguished from one another by matrix composition and topology: (i) particulate alumina bonded by nanoporous silica glass⁵²; (ii) an 80% mullite–20% alumina particle mixture, strengthened by about 4% of a precursor-derived alumina¹²; and (iii) bimodal particulate mullite, with particle sizes of about 1 and 0.1 μm .⁴³ Some additional insights into the extent of sintering are obtained from changes in Young's modulus, plotted in Fig. 18(b). The notable trends follow.

The alumina–silica system undergoes the most rapid degradation, starting at temperatures below 1000°C. In addition to the strength loss, fracture occurs in a brittle manner with virtually no pullout. These changes are correlated with coarsening of matrix porosity and extensive sintering to the fiber surface. Analogous changes are obtained at elevated temperatures and in notched specimens.^{53,54} The retained strength of the system with the mullite–alumina matrix remains essentially unchanged up to 1200°C. Limited sintering is evidenced by elevations in stiffness, especially beyond 1000°C, as well as observations of slightly reduced fiber pullout and larger amounts of remnant matrix on the fiber surfaces.¹² The all-mullite matrix system exhibits the best performance. Its retained strength remains stable up to 1200°C (actually increasing slightly). The stiffness increases over this temperature range, but not as rapidly as that of the mullite–alumina matrix composite. Beyond 1200°C, the stiffness increases at a greater rate and the strength begins to diminish.

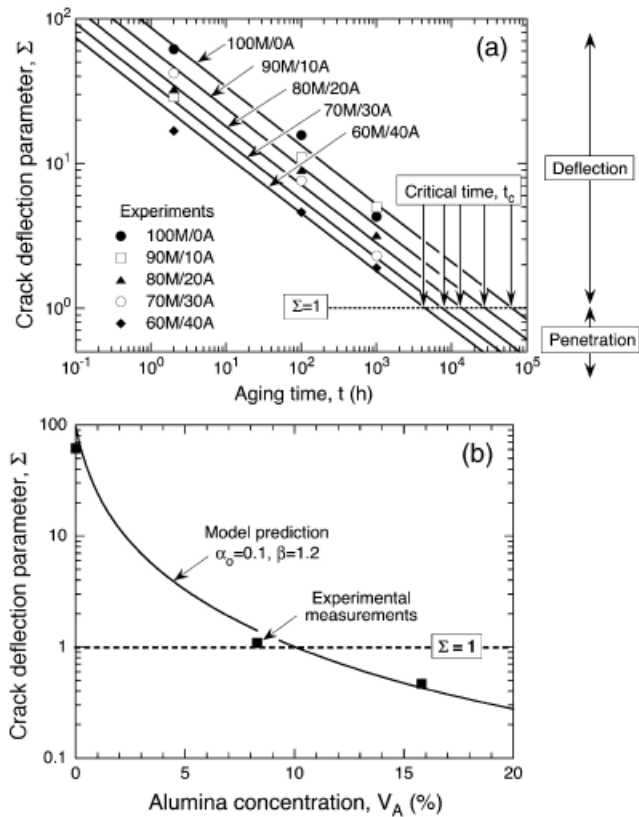


Fig. 17. (a) Effects of aging time and composition in particulate mullite–alumina on the crack deflection parameter Σ , using fiber properties $\Gamma_f = 15 \text{ J/m}^2$ and $E_f = 260 \text{ GPa}$. The solid lines represents model predictions. Extrapolation of the predictions to $\Sigma = \omega \approx 1$ yields the critical time, t_c , at which crack penetration is predicted to occur. (b) Corresponding effects of concentration of precursor-derived alumina in particulate mullite.

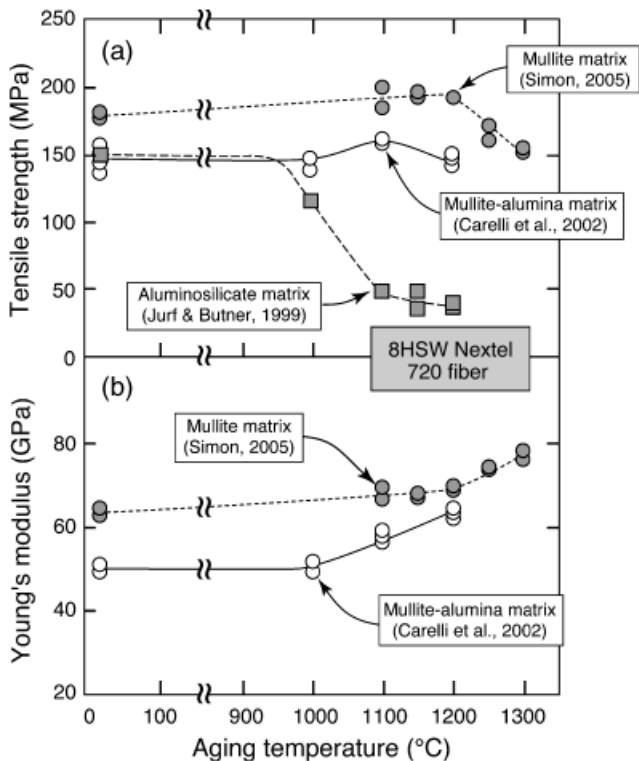


Fig. 18. Effects of matrix composition on the strength retention of Nextel™ 720 fiber composites. (data from^{12,52,43}). Because of slight differences in the fiber volume fractions (ranging from 38% to 45%), strengths have been normalized to a volume fraction of 40%.

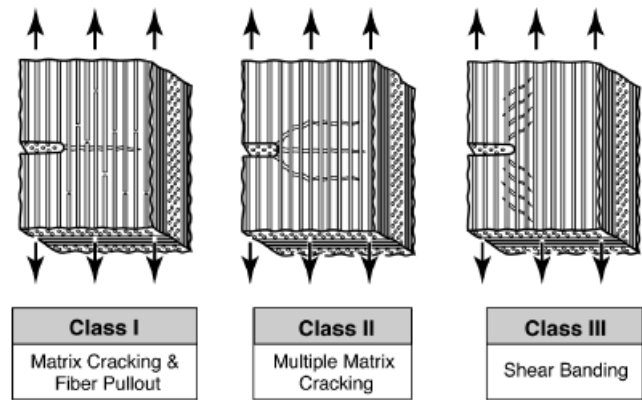


Fig. 19. Classification of damage mechanisms in notched continuous-fiber ceramic composites.

Nevertheless, even after exposure at 1300°C , the composite retains about 80% of its initial strength. The superior performance of this composite is attributable to the enhanced morphological stability of the all-mullite matrix.

VII. Notch Sensitivity

Notch insensitivity is a key attribute of high-performance CFCCs. It allows design of components with complex geometric features and with attendant stress concentrations using principles developed for metallic materials. As with metals, stress concentrations in CFCC structures are mitigated by inelastic deformation, albeit through markedly different mechanisms. Among the dominant modes of deformation experienced by CFCCs (Fig. 19),⁵⁵ Classes I and III are prevalent in the oxides. That is, notched fracture proceeds either by the propagation of a dominant mode I crack, accompanied by fiber bridging, or by the development of shear bands parallel to the direction of loading, followed by fiber rupture. Broadly, the former is characteristic of materials with dense matrices and relatively strong interfaces. It provides the least plastic dissipation and the strongest notch sensitivity. The latter prevails in porous-matrix composites and can mitigate notch sensitivity when the extent of shear banding is large in relation to the notch length.

The state of the matrix plays a dominant role in notch sensitivity, especially in porous-matrix materials. Experimental measurements on three such materials, with varying matrix strength levels, and accompanying photographs of the tested specimens are shown in Figs. 20 and 21(a).⁵⁶ As the strength of the matrix is increased (by addition of a precursor-derived alu-

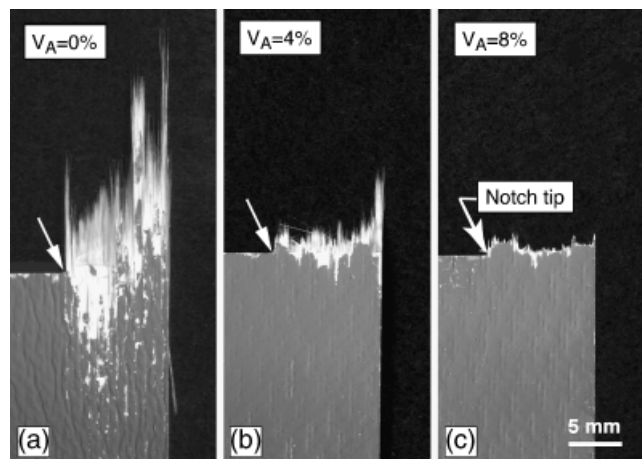


Fig. 20. Macrophotographs of edge-notched tensile specimens, showing the extent of delamination and fiber pullout. Materials consist of Nextel™ 720 fibers in a particulate mullite–alumina matrix, and strengthened by precursor-derived alumina (concentration, V_A). (Adapted from Mattoni and Zok⁵⁶).

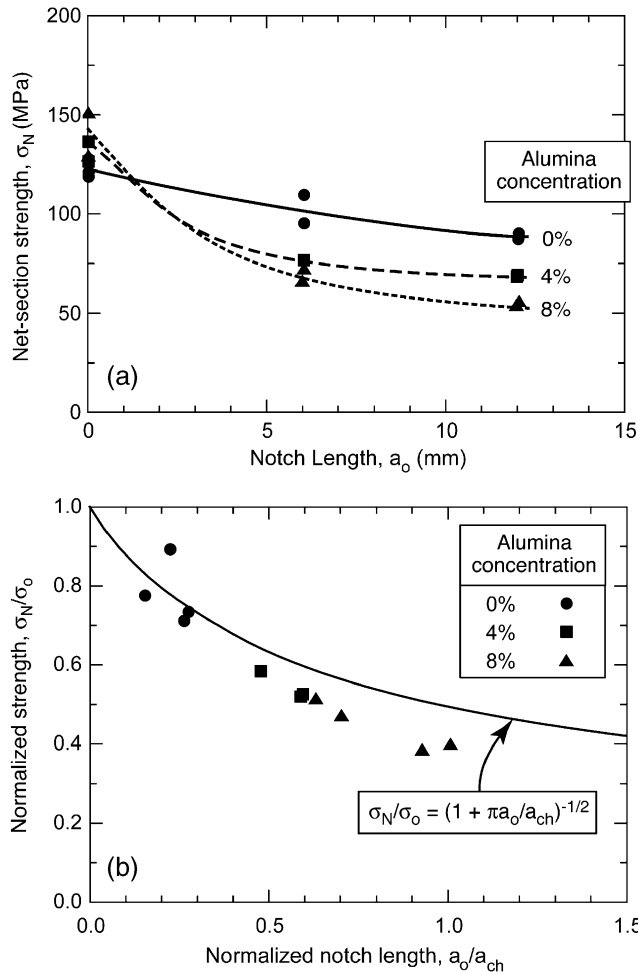


Fig. 21. Notched strength of porous matrix continuous-fiber ceramic composites. (Adapted from Mattoni and Zok⁵⁶).

mina within a particulate mullite–alumina matrix), the length of shear bands emanating from the notch tip and the extent of fiber pullout decrease dramatically. Concurrently, the degree of notch sensitivity increases. For instance, for a notch length of 12 mm, the strength of the composite with the weakest matrix is reduced by only 25% from the unnotched value; in contrast, the one with the strongest matrix exhibits a reduction of 60%.

The notch sensitivity can be rationalized on the basis of established cohesive zone models. In general, the notched strength σ_N is predicted to follow^{57,58}:

$$\frac{\sigma_N}{\sigma_o} = \left(1 + \frac{\pi a_o}{a_{ch}}\right)^{-1/2} \quad (19)$$

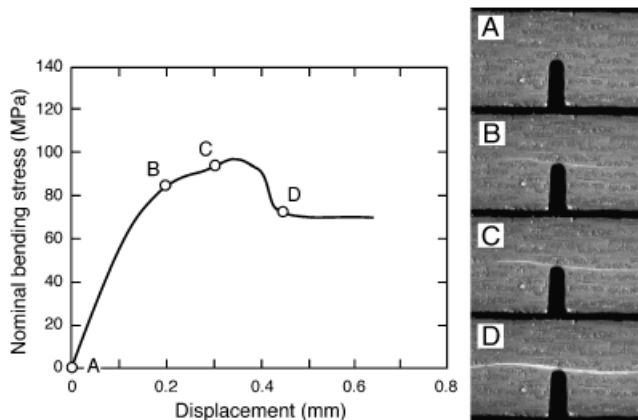


Fig. 22. Delamination in a porous matrix, two-dimensional fabric laminate. (Courtesy J. H. Weaver).

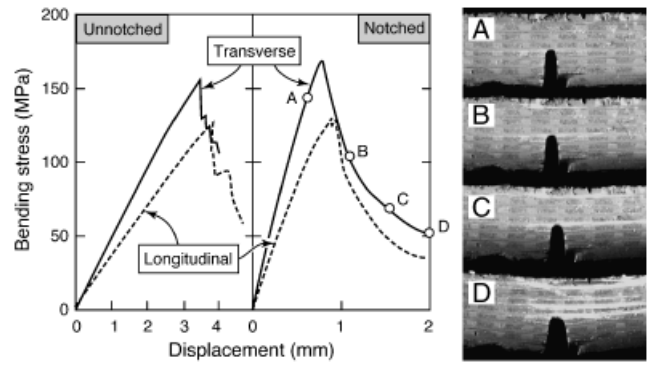


Fig. 23. Notched and unnotched flexural response of a porous matrix, three-dimensional orthogonal weave composite. The fiber volume fractions are 21%, 15%, and 3% in the transverse, longitudinal, and through-thickness directions, respectively (Courtesy J. H. Weaver).

where σ_o is the unnotched tensile strength and a_{ch} is a characteristic length scale, dictated by the work of fracture, the elastic moduli, and the test geometry (details presented in Sidebar C). Upon evaluating the pertinent values of a_{ch} for each of the three composites, the results are re-plotted using the non-dimensional parameters σ_N/σ_o and a_o/q_{ch} (Fig. 21(b)).⁵⁶ In this form, the test results collapse onto essentially a single band, broadly consistent with Eq. (19).

VIII. Delamination

Whether damage tolerance is achieved by porous matrices, weakly bonded coatings, or fugitive coatings, fracture resistance under loads normal to the fiber directions remains low.⁶¹ Laminates of unidirectional tapes or 2D fabrics are particularly vulnerable to delamination. Under mode I and mixed mode I/II loadings (the latter obtained in edge-notched flexure), tape laminates of dense matrix CFCCs (e.g., SiC–fiber glass–ceramics) exhibit an initiation toughness $\approx 20 \text{ J/m}^2$, increasing gradually with increasing crack length and ultimately reaching a steady-state value $\approx 40\text{--}200 \text{ J/m}^2$, dependent on the extent of bridging by in-plane fibers.^{62,63} Similar results have been obtained in porous-matrix CFCCs: the mixed mode toughness being 45–65 J/m^2 at steady state (Fig. 22).

The obvious way to improve delamination resistance is to incorporate through-thickness fibers. Although impressive precedents exist in polymer-matrix composites, oxide CFCCs with 3D fiber architectures remain in their infancy. An illustrative example of a porous matrix reinforced by a 3D orthogonal interlock fiber weave is presented in Fig. 23. With a mere 3% volume fraction of through-thickness fibers, delamination is largely suppressed and the notched strength is essentially identical to the unnotched value. Delamination becomes evident only at large displacements, well beyond that at the peak load. In the latter domain, multiple cracks form between the layers of in-plane fibers and propagate stably from the notch tip.

IX. Concluding Remarks

From their infancy a decade ago, oxide composites have emerged as viable candidates for high-temperature thermostructural applications. Their rapid evolution is attributable to recent developments in materials and microstructural concepts, both for enabling damage tolerance and for ensuring long-term morphological stability at the targeted service temperatures. Among these, the discoveries of monazite as a coating material for oxide fibers and the porous-matrix concept as an alternative to coatings have taken center stage. Alternate strategies for producing weak interfaces as well as cost-effective methods of coating complex fiber architectures are emerging. These are expected to play a significant role in future material designs and their implementation in engineering systems.

Sidebar C. Mechanics of Notch Sensitivity

The mechanics underpinning notched fracture of CFCCs is well established. It is based on continuum descriptions of inelastic deformation, through either cohesive zone models (for Class I and III) or plasticity-type descriptions coupled with an appropriate criterion for fracture initiation (Class II). For the former, two types of cohesive zones are required (Fig. 19). One is aligned parallel to the loading direction and characterized by a shear traction law, $\tau(\delta_s)$; the other is perpendicular, with a tensile traction law, $\sigma(\delta_t)$. In an infinite isotropic notched body, the effective fracture energy Γ is dictated by the interplay between the two bands. That is, when the strength τ_o of the shear zone is small relative to that of the tensile band, σ_o , extensive shear deformation occurs, causing reduction in the peak stress within the tensile band. Otherwise, the tensile band ruptures before shear bands have an opportunity to develop and the fracture energy is the same as that of the tensile band, Γ_o . Pertinent numerical results showing the effects of the strength ratio τ_o/σ_o are plotted on Fig. C1.⁵⁸ Beneficial effects of the shear bands are obtained when $\tau_o/\sigma_o \leq 0.2$.

When the notch length is finite, the condition for composite fracture is again dictated by the interplay between the two bands. Interestingly, when plotted against the normalized notch length, a_o/a_{ch} , with $a_{ch} \equiv \bar{E}\Gamma/\sigma_o^2$, results for the normalized strength fall essentially onto a single, monotonically decreasing band, only weakly dependent on τ_o/σ_o (Fig. C2(b)).⁵⁸ Evidently, the beneficial effects of the shear band are embodied in the fracture energy $\Gamma(\tau_o/\sigma_o)$. The trend is described by the empirical formula in Eq. (19). This formula not only fits the numerical results but also yields the correct values in the limits of very short and very long notches. That is, $\sigma_N/\sigma_o \rightarrow 1$ as $a_o/a_{ch} \rightarrow 0$ (the notch insensitive domain) and $\sigma_N/\sigma_o \rightarrow (\pi a_o/a_{ch})^{-1/2}$ (the Griffith stress) when $a_o/a_{ch} \gg 1$.

Modifications to the analysis must be made to account for finite specimen width and elastic anisotropy.⁵⁶ This is accomplished by re-defining the characteristic length scale a_{ch} such that the predicted strength in the Griffith limit is correct. The result is

$$a_{ch} \equiv \frac{\bar{E}\Gamma}{g(\rho, \lambda)[\sigma_o F(a_o/W)(1 - a_o/W)]^2}$$

where W is specimen width, $F(a_o/W)$ is the usual geometric factor, and $g(\rho, \lambda)$ characterizes the elastic anisotropy.^{59,60} Composites with balanced symmetric fiber lay-ups exhibit cubic in-plane symmetry, whereupon $\lambda \equiv E_1/E_2 = 1$, $\nu_{12} = \nu_{21}$ and $g(\rho, \lambda)$ is given by:

$$g(\rho, \lambda) = \left(\frac{1 + \rho}{2}\right)^{1/2} \times \left(1 + 0.1(1 - \rho) - 0.016(1 - \rho)^2 + 0.002(1 - \rho)^3\right)$$

with

$$\rho \equiv \frac{(E_1 E_2)^{1/2}}{2\mu_{12}} - (\nu_{12}\nu_{21})^{1/2}$$

The subscripts 1 and 2 refer to the principal material axes, μ is the shear modulus, and ν is Poisson's ratio.

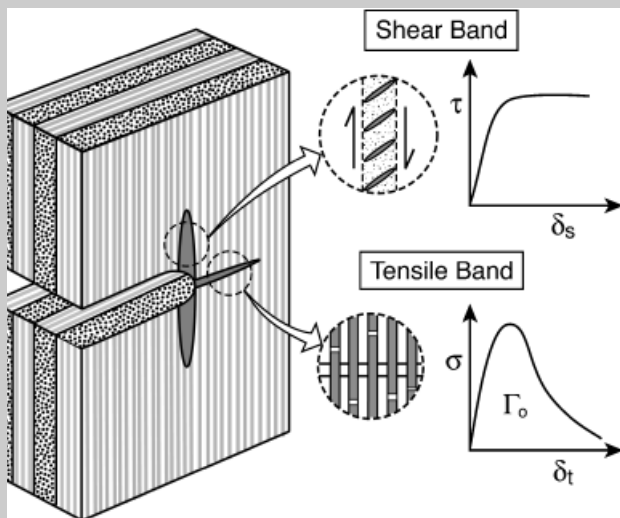


Fig. C1. Notch tip damage processes in porous matrix continuous-fiber ceramic composites.

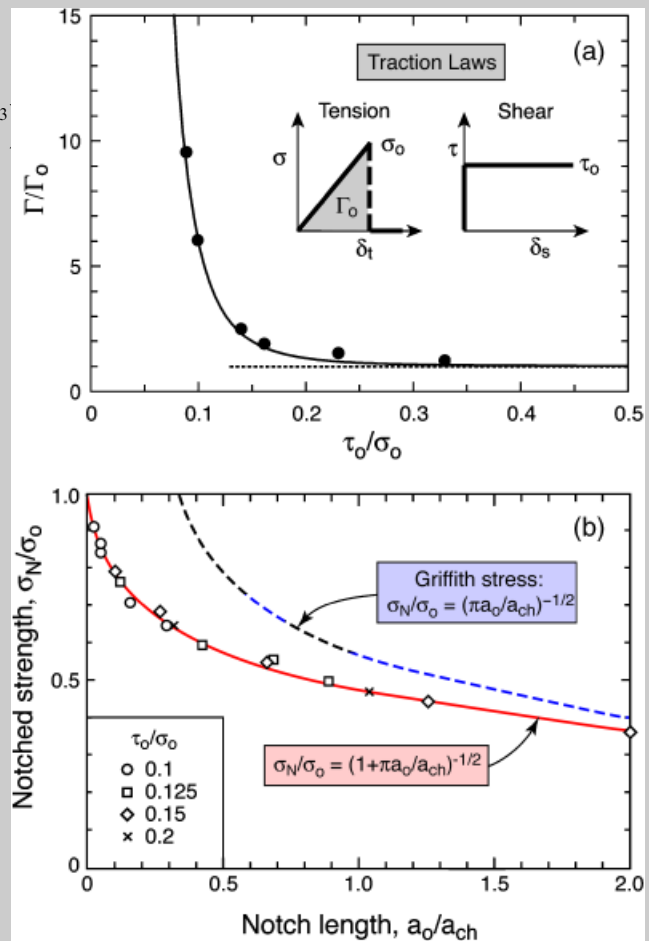


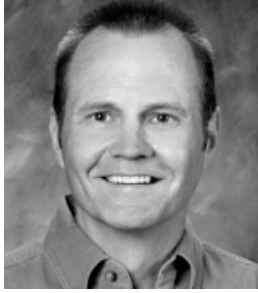
Fig. C2. Effects of strength ratio τ_o/σ_o on (a) composite toughness (infinite-notched body) and (b) tensile strength (edge-notched semi-infinite body). (Adapted from Suo *et al.*⁵⁷ and He *et al.*⁵⁸).

Acknowledgment

The author gratefully acknowledges important contributions to this work from Carlos G. Levi, George Jefferson, Hiroki Fujita, Jared H. Weaver, James Yang, and Michael A. Mattoni.

References

- ¹R. C. Robinson and J. L. Smialek, "SiC Recession Caused by SiO₂ Scale Volatility Under Combustion Conditions: I. Experimental Results and Empirical Model," *J. Am. Ceram. Soc.*, **82**, 1817–25 (1999).
- ²E. J. Opila, J. L. Smialek, R. C. Robinson, D. S. Fox DS, and N. S. Jacobson, "SiC Recession Caused by SiO₂ Scale Volatility Under Combustion Conditions: II. Thermodynamics and Gaseous Diffusion Model," *J. Am. Ceram. Soc.*, **82**, 1826–34 (1999).
- ³N. S. Jacobson, E. J. Opila, and K. N. Lee, "Oxidation and Corrosion of Ceramics and Ceramic Matrix Composites," *Curr. Opin. Solid State Mater. Sci.*, **5**, 301–9 (2001).
- ⁴R. J. Kerans, R. S. Hay, T. A. Parthasarathy, and M. K. Cinibulk, "Interface Design for Oxidation-Resistant Ceramic Composites," *J. Am. Ceram. Soc.*, **85**, 2569–632 (2002).
- ⁵W. C. Tu, F. F. Lange, and A. G. Evans, "Concept for a Damage-Tolerant Ceramic Composite With Strong Interfaces," *J. Am. Ceram. Soc.*, **79** [2] 417–24 (1996).
- ⁶A. Szweda, M. L. Millard, and M. G. Harrison, "Fiber Reinforced Ceramic Matrix Composites and Method for Making U.S. Patent 5,601,674, 1997.
- ⁷F. F. Lange, W. C. Tu, and A. G. Evans, "Processing of Damage-Tolerant, Oxidation Resistant Ceramic-Matrix Composites by a Precursor Infiltration and Pyrolysis Method," *Mater. Sci. Eng. A*, **195**, 145–50 (1995).
- ⁸C. G. Levi, J. Y. Yang, B. J. Dalgleish, F. W. Zok, and A. G. Evans, "Processing and Performance of an All-Oxide Ceramic Composite," *J. Am. Ceram. Soc.*, **81**, 2077–86 (1998).
- ⁹J. A. Heathcote, X. Y. Gong, J. Y. Yang, U. Ramamurty, and F. W. Zok, "In-Plane Mechanical Properties of an All-Oxide Ceramic Composite," *J. Am. Ceram. Soc.*, **82** [10] 2721–30 (1999).
- ¹⁰B. Kanka and H. Schneider, "Aluminosilicate Fiber/Mullite Mullite Composites With Favorable High-Temperature Properties," *J. Eur. Ceram. Soc.*, **20** [14–15] 619–23 (2000).
- ¹¹M. A. Mattoni, J. Y. Yang, C. G. Levi, and F. W. Zok, "Effects of Matrix Porosity on the Mechanical Properties of a Porous-Matrix, All-Oxide Ceramic Composite," *J. Am. Ceram. Soc.*, **84**, 2594–602 (2001).
- ¹²E. A. V. Carelli, H. Fujita, J. Y. Yang, and F. W. Zok, "Effects of Thermal Aging on the Mechanical Properties of a Porous-Matrix Ceramic Composite," *J. Am. Ceram. Soc.*, **85** [3] 595–602 (2002).
- ¹³J. B. Davis, J. P. A. Lofvander, A. G. Evans, E. Bischoff, and M. L. Emiliani, "Fiber Coating Concepts for Brittle-Matrix Composites," *J. Am. Ceram. Soc.*, **76**, 1249 (1993).
- ¹⁴T. J. Mackin, J. Y. Yang, C. G. Levi, and A. G. Evans, "Environmentally Compatible Double Coating Concepts for Sapphire Fiber-Reinforced γ -TiAl," *Mater. Sci. Eng.*, **A161**, 285–93 (1993).
- ¹⁵A. G. Evans and F. W. Zok, "The Physics and Mechanics of Fibre-Reinforced Brittle Matrix Composites," *J. Mater. Sci.*, **29**, 3857–96 (1994).
- ¹⁶K. A. Keller, T. Mah, T. A. Parthasarathy, and C. Cooke, "Fugitive Interfacial Carbon Coatings for Oxide/Oxide Composites," *Ceram. Eng. Sci. Proc.*, **14**, 878–79 (1993).
- ¹⁷K. A. Keller, T. Mah, T. A. Parthasarathy, and C. M. Cooke, "Fugitive Interfacial Carbon Coatings for Oxide/Oxide Composites," *J. Am. Ceram. Soc.*, **83** [2] 329–36 (2000).
- ¹⁸J. B. Davis, J. P. A. Lofvander, A. G. Evans, E. Bischoff, and M. L. Emiliani, "Fiber Coating Concepts for Brittle Matrix Composites," *J. Am. Ceram. Soc.*, **76** [5] 1249–57 (1993).
- ¹⁹D. M. Wilson, "Statistical Tensile Strength of Nextel 610 and Nextel 720 Fibres," *J. Mater. Sci.*, **32** [10] 2535–42 (1997).
- ²⁰P. E. D. Morgan and D. B. Marshall, "Ceramic Composites of Monazite and Alumina," *J. Am. Ceram. Soc.*, **78** [6] 1553–63 (1995).
- ²¹D. B. Marshall, P. E. D. Morgan, R. M. Housley, and J.T. Cheung, "High Temperature Stability of the Al₂O₃-LaPO₄ System," *J. Am. Ceram. Soc.*, **81** [4] 951–6 (1998).
- ²²D. B. Marshall, J. B. Davis, P. E. D. Morgan, and J. R. Porter, "Interface Materials for Damage-Tolerant Oxide Composites," *Key Eng. Mater.*, **127–131**, 27–36 (1997).
- ²³R. S. Hay, "Monazite and Scheelite Deformation Mechanisms," *Ceram. Eng. Sci. Proc.*, **21** [4] 203–28 (2000).
- ²⁴J. B. Davis, R. S. Hay, D.B. Marshall, P. E. D. Morgan, and A. Sayir, "Influence of Interfacial Roughness on Fiber Sliding in Oxide Composites with Laminate Interphases," *J. Am. Ceram. Soc.*, **86** [2] 305–16 (2003).
- ²⁵D.-H. Kuo and W. M. Kriven, "Characterization of Yttrium Phosphate and a Yttrium Phosphate/Yttrium Aluminate Laminate," *J. Am. Ceram. Soc.*, **78** [11] 3121–4 (1995).
- ²⁶M. G. Cain, R. L. Cain, A. Tye, P. Rian, M. H. Lewis, and J. Gent, "Structure and Stability of Synthetic Interphases in CMCs," *Key Eng. Mater.*, **127–131**, 37–49 (1997).
- ²⁷M. H. Lewis, A. Tye, E. G. Butler, and P. A. Doleman, "Oxide CMCs: Interphase Synthesis and Novel Fibre Development," *J. Eur. Ceram. Soc.*, **20**, 639–44 (2000).
- ²⁸E. Boakye, R. S. Hay, and M. D. Petry, "Continuous Coating of Oxide Fiber Tows Using Liquid Precursors: Monazite Coatings on Nextel 720," *J. Am. Ceram. Soc.*, **82** [9] 2321–31 (1999).
- ²⁹R. S. Hay and E. Boakye, "Monazite Coatings on Fibers: I, Effect of Temperature and Alumina Doping on Coated-Fiber Tensile Strength," *J. Am. Ceram. Soc.*, **84** [12] 2783–92 (2001).
- ³⁰E. Boakye, R. S. Hay, P. Mogilevsky, and L. M. Douglas, "Monazite Coatings on Fibers: II, Coating Without Strength Degradation," *J. Am. Ceram. Soc.*, **84** [12] 2793–801 (2001).
- ³¹R. S. Hay and E. E. Hermes, "Coating Apparatus for Continuous Fibers U.S. Patent No. 5 217 533, 1993.
- ³²R. S. Hay, "Method for Coating Continuous Tows U.S. Patent No. 5,164,229, 1993.
- ³³K. A. Keller, T. Mah, T. A. Parthasarathy, E. E. Boakye, P. Mogilevsky, and M. K. Cinibulk, "Effectiveness of Monazite Coatings in Oxide/Oxide Composites After Long-Term Exposure at High Temperature," *J. Am. Ceram. Soc.*, **86** [2] 325–32 (2003).
- ³⁴J. H. Weaver, J. Y. Yang, C. G. Levi, F. W. Zok, and J. B. Davis, "A Method for Coating Fibers in Oxide Composites," (to be published).
- ³⁵J. B. Davis, D. B. Marshall, and P. E. D. Morgan, "Oxide Composites of Al₂O₃ and LaPO₄," *J. Eur. Ceram. Soc.*, **19**, 2421–6 (1999).
- ³⁶J. M. Staehler and L. P. Zawada, "Performance of Four Ceramic-Matrix Composite Divergent Flap Inserts Following Ground Testing on an F110 Turbofan Engine," *J. Am. Ceram. Soc.*, **83**, 1727–38 (2000).
- ³⁷M.-Y. He and J. W. Hutchinson, "Crack Deflection at an Interface Between Dissimilar Elastic Materials," *Int. J. Solids Struct.*, **25** [9] 1053–67 (1989).
- ³⁸F. Zok, F. F. Lange, and J. R. Porter, "Packing Density of Composite Powder Mixtures," *J. Am. Ceram. Soc.*, **74** [8] 1880–5 (1991).
- ³⁹C. G. Levi, F. W. Zok, J. Y. Yang, M. Mattoni, and J. P. A. Lofvander, "Microstructural Design of Stable Porous Matrices for All-Oxide Ceramic Composites," *Z. Metallkd.*, **90** [12] 1037–47 (1999).
- ⁴⁰H. Fujita, G. Jefferson, C. G. Levi, and F. W. Zok, "Controlling Mechanical Properties of Porous Mullite/Alumina Mixtures Via Precursor-Derived Alumina," *J. Am. Ceram. Soc.*, **88** [2] 367–75 (2005).
- ⁴¹F. W. Zok, "Fracture Analysis of Fiber-Reinforced Ceramic Composites"; pp. 407–18 in *ASM International Engineered Materials Handbook, Vol. 1: Composites*, 2nd edition, ASM International, Materials Park, OH 2001.
- ⁴²H. Fujita, G. Jefferson, R. M. McMeeking, and F. W. Zok, "Mullite-Alumina Mixtures for Use as Porous Matrices in Oxide Fiber Composites," *J. Am. Ceram. Soc.*, **87** [2] 261–7 (2004).
- ⁴³R. A. Simon, "Progress in Processing and Performance of Porous-Matrix Oxide/Oxide Composites," *Int. J. Appl. Ceram. Technol.*, **2** [2] 141–9 (2005).
- ⁴⁴M. F. Ashby, "A First Report on Sintering Diagrams," *Acta Metall.*, **22** [3] 275–89 (1974).
- ⁴⁵R. M. German, "Fundamentals of Sintering"; pp. 260–9 in *Ceramics and Glasses, Engineered Materials Handbook, Vol. 4*, ASM International, Materials Park, OH (1991).
- ⁴⁶K. Walton, "The Effective Elastic Moduli of a Random Packing of Spheres," *J. Mech. Phys. Solids*, **35** [2] 213–26 (1987).
- ⁴⁷G. Jefferson, G. K. Haritos, and R. M. McMeeking, "The Elastic Response of a Cohesive Aggregate—A Discrete Element Model with Coupled Particle Interaction," *J. Mech. Phys. Solids*, **50** [12] 2539–75 (2002).
- ⁴⁸D. J. Green, C. Nader, and R. Brezny, "The Elastic Behavior of Partially-Sintered Alumina"; pp. 345–56 in *Sintering of Advanced Ceramics*, Edited by C. A. Handwerker, J. E. Blendell, and W. Kaysser. American Ceramic Society, Westerville, OH, 1990.
- ⁴⁹K. L. Johnson, *Contact Mechanics*. Cambridge University Press, Cambridge, 1985.
- ⁵⁰D. B. Marshall and W. C. Oliver, "Measurement of Interfacial Mechanical Properties in Fiber-Reinforced Ceramic Composites," *J. Am. Ceram. Soc.*, **70** [8] 542–8 (1987).
- ⁵¹J. H. Weaver, J. Rannou, M. A. Mattoni, and F. W. Zok, "Interface Properties in a Porous-Matrix Oxide Composite," *J. Am. Ceram. Soc.*, **89** [9] 2869–73.
- ⁵²R. A. Jurf and S. C. Butner, "Advances in Oxide-Oxide CMC," *J. Eng. Gas Turb. Power*, **122** [2] 202–5 (2000).
- ⁵³V. A. Kramb, R. John, and L. P. Zawada LP, "Notched Fracture Behavior of an Oxide/Oxide Ceramic-Matrix Composite," *J. Am. Ceram. Soc.*, **82** [11] 3087–96 (1999).
- ⁵⁴L. P. Zawada, R. S. Hay, S. S. Lee, and J. Staehler, "Characterization and High Temperature Mechanical Behavior of an Oxide/Oxide Composite," *J. Am. Ceram. Soc.*, **86** [6] 981–90 (2003).
- ⁵⁵A. G. Evans and F. W. Zok, "The Physics and Mechanics of Fibre-Reinforced Brittle Matrix Composites," *J. Mater. Sci.*, **29**, 3857–96 (1994).
- ⁵⁶M. A. Mattoni and F. W. Zok, "Strength and Notch Sensitivity of Porous-Matrix Oxide Composites," *J. Am. Ceram. Soc.*, **88** [6] 1504–13 (2005).
- ⁵⁷Z. Suo, S. Ho, and X. Gong, "Notch Ductile-to-Brittle Transition Due to Localized Inelastic Band," *J. Eng. Mater. Technol.*, **115** [3] 319–26 (1993).
- ⁵⁸M.-Y. He, B. Wu, and Z. Suo, "Notch-Sensitivity and Shear Bands in Brittle Matrix Composites," *Acta Metall. Mater.*, **42** [9] 3065–70 (1994).
- ⁵⁹Z. Suo, G. Bao, B. Fan, and T. C. Wang, "Orthotropy Rescaling and Implications for Fracture in Composites," *Int. J. Solids Struct.*, **28** [2] 235–48 (1991).
- ⁶⁰G. Bao, S. Ho, Z. Suo, and B. Fan, "The Role of Material Orthotropy in Fracture Specimens for Composites," *Int. J. Solids Struct.*, **29** [9] 1105–16 (1992).
- ⁶¹L. P. Zawada, "Longitudinal and Transthickness Tensile Behavior of Several Oxide/Oxide Composites," *Ceram. Eng. Sci. Proc.*, **19** [3] 327–39 (1998).
- ⁶²O. Sbaizer, P. G. Charalambides, and A. G. Evans, "Delamination Cracking in a Laminated Ceramic-Matrix Composite," *J. Am. Ceram. Soc.*, **73** [7] 1936–40 (1990).
- ⁶³S. M. Sparing and A. G. Evans, "The Role of Fiber Bridging in the Delamination Resistance of Fiber-Reinforced Composites," *Acta Metall. Mater.*, **40** [9] 2191–9 (1992). □



Frank Zok is Professor and Associate Chair of the Materials Department at the University of California at Santa Barbara. He obtained his Ph.D. degree from McMaster University, Canada, in Materials Engineering in 1988 and joined the faculty at the University of California in 1990. His research interests concern design, synthesis and mechanical performance of engineering materials. Most recently, his research has focused on high temperature ceramic composites, topological design of lightweight metallic sandwich structures, and tribological and mechanical behavior of biological systems. Dr. Zok has served as Associate Editor for the *Journal of the American Ceramic Society* since 1993. He is the author of over 130 peer-reviewed scientific papers.